2020

Engineering the Surface Chemistry and Surface Conditions to Optimize the Heat Removal Rate of Various Surfaces

Thomas Germain
University of Central Florida

ENGINEERING THE SURFACE CHEMSITRY AND SURFACE CONDITIONS TO OPTIMIZE THE HEAT REMOVAL RATE OF VARIOUS SURFACES

by

THOMAS MICHAEL GERMAIN
B.S.M.E. University of South Florida, 2016

A dissertation submitted in partial fulfilment of the requirements
for the degree of Doctor of Philosophy
in the Department of Mechanical and Aerospace Engineering
in the College of Engineering and Computer Science
at the University of Central Florida
Orlando, Florida

Fall Term
2020

Major Professor: Shawn A. Putnam

ABSTRACT

As the demand for more powerful and smaller electronics rise, the need for creative cooling solutions to prevent burnout becomes increasingly paramount. In response to recent cooling needs, new cooling techniques, such as jet impingement cooling, spray cooling, and heat pipes, have risen in popularity for their simple design and efficiency in thermal transport. This interest has risen in both industry and academia, where research has been conducted to optimize the heat transfer performance for these systems and how these systems can be implemented in new technologies. One method that has risen in interest is affecting the surface, through physical and chemical treatments, and how these different treatments can enhance the heat removal rate for different systems.

This dissertation presents two main regions of research that, when combined, can enhance understanding of cooling rates for different surface treatments. The first region is utilizing time domain thermoreflectance (TDTR) to measure the heat transfer coefficients in a microchannel experiencing jet impingement cooling. This current study presents the findings of experiments that measure the heat transfer coefficients on surfaces exposed to hot-spot heating and cooled using water jet impingement at Reynolds numbers up to 6432. The heat transfer coefficients were found using TDTR with a water jet on a fused silica (FS) glass substrate coated with a thin-film Hafnium-alloy (Hf). The heat transfer coefficient data are based on a local, micron-sized hot-spot region (generated by the TDTR pump laser) that is translated at different locations relative to the stagnation point. The study shows that at different microchannel regions (relative to the stagnation point) and for different Reynolds numbers for the jet that the TDTR method can detect changes in the heat transfer coefficient.

Along with a novel method to measure the heat transfer coefficients using TDTR, several studies on different surface conditions are presented in the dissertation. Physical changes in wetting

performance is analyzed through soft wetting materials and the impact the stiffness has on the hemwicking performance. Through a novel, in house stamping apparatus, polydimethylsiloxane (PDMS) samples were created of varing stiffness of 0.338 MPa to 1.98 MPa. Through analyzing the hemiwicking velocity, hemiwicking diffusion, and initial hemiwicking wicking velocity of ethanol, isopropyl alcohol, and isooctane, it was observed that the stiffness of soft materials can play a significant impact on the overall wicking performance. Furthermore, a deformation model is presented based on pillar deformations observed with PDMS/ExoFlex hybrid samples as the working fluids evaporated from the wicking arrays.

The chemical impact on the overall wetting performance is also analyzed and presented in this dissertation. Two main methods were implemented to track the changes in wetting through surface chemistry; through the application of a polyvinyl alcohol (PVA) self-assembled monolayer (SAM) and applying a spiropyran (SPCOOH) to a microstructured gold surface. The changes in hemiwicking velocity and meniscus extension with the PVA SAM displayed an important aspect of chemical interactions with respect to hemiwicking performance, which affects the heat transfer performance of a microstructured surface. The SPCOOH studies revealed a change in wetting behavior which further emphasized the importance of intermolecular interaction on wetting performance, but also revealed a controlling aspect the PVA SAM experiments did not exhibit.

Along with these studies, a preliminary study of controlling the intermolecular interactions of metamaterials through strain to change the surface wetting is presented in this dissertation. Through the use of a simple, uni-axial strain instrument, different metamaterials composed of hafnium dioxide, titanium nitride, and tungsten deposited on Kapton tape were subjected to strains up to 8%. While under strain, significant changes in the advancing, receding, and equilibrium contact angle were observed for both polar and non polar fluids on the surface. These changes are attributed through changes in the intermolecular forces and verified through changes in the reflectivity while strain is applied to the metamaterials.

To my family, whose endless support and encouragement have made this work possible

ACKNOWLEDGMENTS

First and foremost, I would like to give thanks and praise to God. During my time of study, I have been constantly blown away by how complex things that appear simple actually are; displaying the immense wisdom, power, and creativity of the God we serve. I am beyond blessed and thankful for this time and all glory and praise belongs to God alone.

I would like to thank my wife, Lauren, for being there every step of the way. I'm beyond blessed and thankful to share this life with you. Thank you so much for sharing in all my excitements with good results in research, encouraging me when hard times arose during my time as a graduate student, pressing me to be a better person every step of the way, and loving me through everything. I am beyond happy to share this moment with you.

I would like to thank my family, namely my mom, dad, Sarah, Casey, Zach, grandma Vesey, grandpa Elmore, and grandpa Germain. Thank you for the constant love and support during this time and for all the life lessons that you have taught me along the way.

I would also like to extend thanks to my advisor, Dr. Shawn Putnam, for not just teaching me how to become an subject matter expert and a great researcher, but how to be a great manager, mentor, and husband. I will cherish our conversations about faith for all my days and thank you for always pushing me to be the best I can be even when I had doubts with myself.

I would also like to thank my committee members, Dr. Louis Chow, Dr. Yoav Peles, and Dr. Karin Chumbimuni-Torres, for all of their insight and assistance for this dissertation.

I would also like to thank my labmates throughout my time as a doctoral student; Dr. Mehrdad Mehrvand, Tanvir Ahmed Chowdhury, Khan Mohammad Rabbi, Krishnan Manoharan Siva Rama, Chance Brewer, Armando Arends, Jimmy Owens, Mateo Gomez, Danny Croatti, and John Bal.

Thank you for all the insight in my work and the memories that we shared being able to research together the past few years. I would also like to acknowledge Parth Patel and Ali Haghighat Mesbahi for all their expertise and assistance with the chemistry aspects of this dissertation.

A special acknowledgement goes to Jake Carter and his work at the Air Force Research Lab in Dayton, Ohio. Without his work in the lab, the metamaterials experiments and aspects of the spiropyran experiments would not have been possible. Along with his work in fabricating the samples, his assistance in experimentation and theory was beneficial to the work presented in this work.

TABLE OF CONTENTS

LIST OF FIGURES

LIST OF TABLES

CHAPTER 1: INTRODUCTION

Background and Motivations

Future Heat Transfer Requirements

As the desire for more powerful and more compact electronic devices increases, the need for more efficient cooling systems are required to prevent burnout and failure [1, 2]. In fact, Mitsutake et al. estimates that the cooling flux needs will need to increase from the current 10 MW/m^2 to 100 MW/m^2 [3]. One important and well respected statement that reflects that need for improved cooling methods is Moore's Law, which states that the amount of chips per semiconductor integrated circuit will double every two years [4, 5]. As the number of components increases, the power dissipated will also increase, explaining the need for better cooling on these electronic systems. However, as Moore's Law still hold true and the power dissipation increases, the amount of cooling possible leveled off, leading to an increase in the need for greater heat transfer innovation and research [6].

Current Popular Responses and Solutions

As a result of these thermal needs, various different cooling technologies have arisen to meet the thermal demands. Some of these technologies include jet impingement, spray cooling, and microchannel flow [7, 6, 8, 9, 10]. Table 1.1 provides a summary of some of the heat transfer coefficients recorded using some of these modern techniques [11, 12, 13, 14, 15, 16, 17, 18]. It can be observed from the table that the modern cooling methods do provide a greater cooling rate than traditional cooling systems. Along with the orientation of the fluid flow, modern cooling systems

achieve higher cooling rates through utilizing two phase flow [19, 20, 21]. As a result of these findings, research has been conducted to fully utilize these modern heat transfer techniques for future technologies.

Table 1.1: The Measured Heat Transfer Coefficients of Micro-scale Cooling Methods in Recent Research

Cooling Method	Microchannels (Single-Phase)		Microchannels (Boiling)		Jet Impingement (Single-Phase)			Jet Impingement (Boiling)	
Fluid	Water	Refrigerant	Water	Refrigerant	Water	Refrigerant	Air	Water	Refrigerant
$h(\frac{kW}{m^2-K})$	10-500	1-30	20-200	2-100	30-320	40-400	5-400	200-1000	50-120

Along with the aforementioned cooling systems, heat pipes have emerged as a popular method of thermal management in modern design [22, 23, 24, 25]. A heat pipe is a simple device where a material of high thermal conductivty that is connected to a heated surface (i.e. evaporator) and a heat sink (i.e. compressor). Due to the high thermal transport ability of the material used, the temperature gradient across the heat pipe will be relatively small, making the system effective in cooling heated regions of interest [24]. The effectiveness and simplicity of this system has made this form of thermal transport popular for a wide range of applications, including photovoltaic cells, air conditioning, and micro-electro-mechanical system (MEMS) [26, 27, 28]. A subsection of heat pipes that have recently risen in popularity is the usage of flexible heat pipes [29, 30]. This need for flexible heat pipes have risen due to the increase in complicated geometries used in modern technology, particularly in the fields of foldable electronics and spacecraft radiators [31, 32].

Surface Wetting

Another important aspect of maximizing the possible heat transfer removal from the surface is understanding the liquid-surface interactions. This has revealed itself in different aspects of heat transfer, but most notably through the evaporating meniscus extension of a fluid [33, 34, 35]. However, a region of interest that has risen within surface wetting in the heat transfer community

is the hydrophilicity of a surface. Since the initial speed of wetting has shown to be important in estimating the maximum thermal transport a fluid can perform on a surface, investigations of taken place on how the hydrophilicity of a surface impacts the heat transfer [36, 37, 38]. Through these findings, it has become important to understand the molecular interactions between a liquid and a surface and what can be done to optimize the thermal transport.

One of the main manufacturing techniques used on heat pipes to increase the cooling performance of the cooling system is fabricating micro and nano sized structures to help induce wetting [39, 40]. The enhanced surface wetting that occurs due to the capillary forces brought upon by the micro and nano sized structures is commonly known as hemiwicking [41, 42]. This is a great advantage for modern technologies since hemiwicking acts like a fluid pump on a surface without any moving parts. Utilizing these structures have become popular since it has been established that these structures can help increase the critical heat flux a surface can experience [43, 39].

Approach and Outline

Due to the popularity of micro and nano scale heat transfer for cooling, this work will introduce research performed for a variety of modern cooling techniques with ways to improve upon already popular heat transfer systems. First, a new method to measure the heat transfer coefficients in a microchannel experiencing jet impingement cooling using a pump-probe optical method will be introduced. This method, first introduced by Mehrvand et al., is useful to finding the cooling conditions within the thermal boundary layer at different locations along the microchannel [44]. With a method to determine the cooling performance of a popular modern cooling technique introduced, different methods of improving cooling on the surface will be analyzed. The methods introduced to increase the cooling rate on the surface rate will be based on the idea of enhancing the surface wetting that occurs, namely through hemiwicking and controllable wetting. Under the idea of con-

trollable wetting, two main aspects are going to be investigated; changes in surface energy with metamaterials and the use of photosensitive coatings.

The next chapter will dive deeper into what other research groups have done and the physics and chemistry behind jet impingement, hemiwicking, metamaterials, and photoreactive compounds. With the literature review established, the following chapter will dive into the research methodology implemented for the different aspects covered in this dissertation. After the research methodology, the individual results from the different research fields will be discussed. Lastly, with all of the findings in this dissertation presented, a synthesis of the the findings will be performed to outline the significance of the work presented in this dissertation; novel methods to increase the cooling rates in modern cooling technologies utilizing optical techniques to measure the heat transport within the thermal boundary layer.

CHAPTER 2: JET IMPINGEMENT HEAT TRANSFER

Literature Review

In academia and industry, jet impingement has risen as a popular cooling system in recent decades. This rise in popularity is due to the higher heat transfer coefficients that are recorded with jet impingement systems along with the need for increased heat removal to prevent burnout in recent inventions [1, 2]. As a result of the promising initial results, a great amount of experimentation has been conducted to discover the optimal design for jet impingement systems to get the most efficient cooling and where the most cooling will occur.

Figure 2.1 provides a schematic of a jet impingement system cooling a heated plate. When discussing jet impingement cooling systems, it is important to understand the different regions within the system. First, as the fluid exits the nozzle and joins the jet, shearing begins to occur on the sides

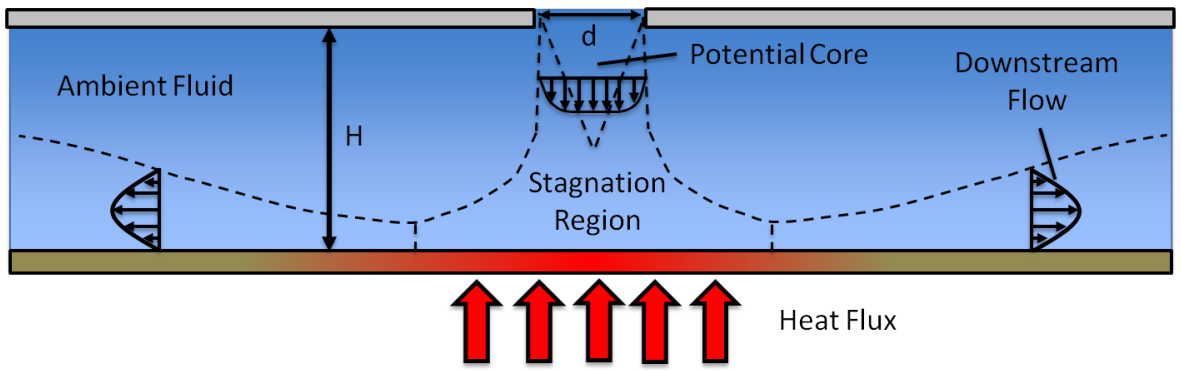

Figure 2.1: A schematic of a jet impingement cooling system with the important geometric definitions when designing this cooling system.

of the exiting fluid. This region between the exit of the nozzle and the heated surface is known as the free jet region [45]. During the free jet region, two regions begin to develop based on the shear penetration into the jet; the potential core and the shear layer [46]. The potential core refers to the region where the shear penetration has not impacted the flow, creating an inviscid flow region as the fluid approaches that heated surface [47]. In contrast, the shear layer is the section of fluid where shear affects of interactions with the ambient fluid affect the jet flow as the jet approaches the surface [46]. If the shear penetrates the entire jet approaching the surface, a decaying jet is formed, where the velocity and pressure of the jet begin to decrease due to the shear forces interacting throughout the jet. Main contributors to the behavior of the potential core and the shear layer are the distance between the jet outlet and the surface and the initial velocity of the jet out of the outlet [48].

As the jet comes into contact with the heated surface, three main regions of interest arise with differing physics and fluid dynamics. The first region is the stagnation region, which is defined as the region beneath the jet outlet where the fluid velocity is assumed to be zero. This region is of particular interest in jet impingement cooling systems since the maximum cooling rates are typically observed within the stagnation region [49]. Surrounding the stagnation region is the acceleration region, the section of the flow where the flow direction begins to transition from normal to the surface to parallel to the surface [49]. Lastly, the radial region is the region where the fluid velocity is parallel to the surface [49]. Within the radial region, the boundary layer of the fluid increases rapidly as the fluid travels down the plate. This occurs due to the decrease in velocity of the fluid that occurs within this region [50, 51].

Various experiments have been conducted considering the optimal geometric (i.e. d_{jet},h) conditions to optimize the heat removal rate. One important parameter that has risen out of research is the ratio of the distance between the jet and the heated surface to the diameter of the jet diameter. Studies have found that the optimal ratio lies between 2 and 6 (h/d_{jet}) [45, 52]. This is due to

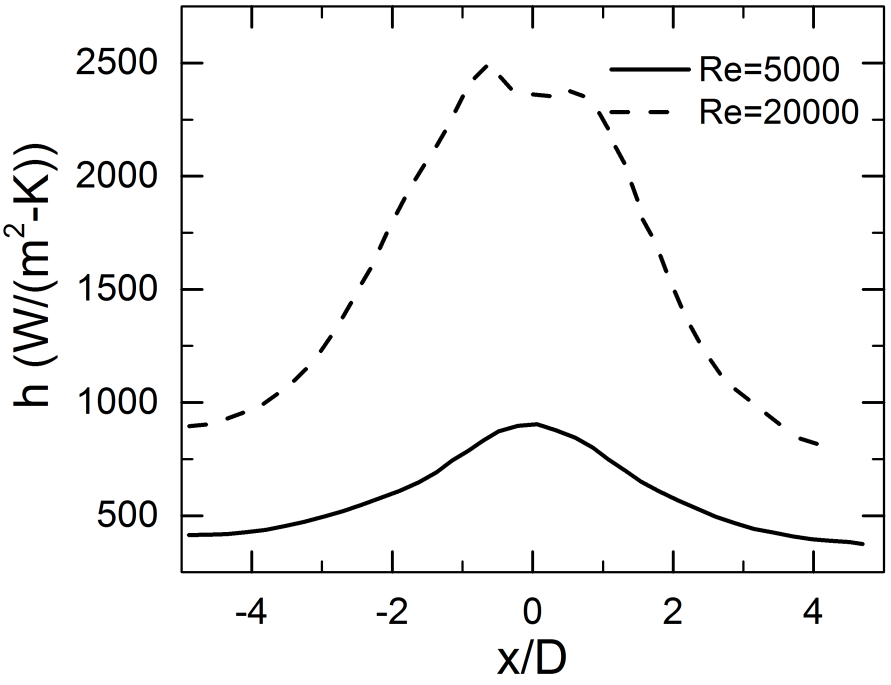

Figure 2.2: Data of jet impingement cooling from experiments by Glynn et al. at twodifferent Reynolds numbers. The diameter of the jet is 1.5 mm and H/d_{jet} is 2

the developing region discussed earlier in this section. If $h/d_{jet} > 6$, the decaying region begins to impede on the jet velocity and decreases the thermal transport for the cooling system. On the contrary, for cases where $h/d_{jet} < 2$, the jet does not have enough space to fully develop, leading to a less efficient cooling rate [45]. Along with this parameter, the geometries of the jet have been investigated. Interestingly, it has been shown that the geometry of the jet, outside of the effective diameter of the jet, does not play a significant impact in the thermal transfer in a jet impingement system [53].

However, some interesting findings have risen based off of investigations between differing flow conditions for jet impingement systems. One of the main interesting findings comes from the dif-

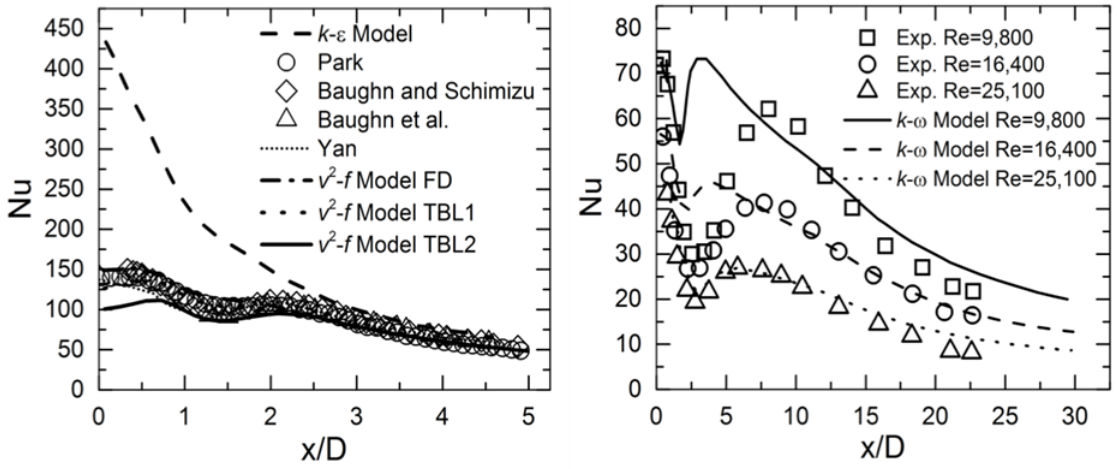

Figure 2.3: Comparisons of the recorded Nusselt number for different jet impingement experiments compared to various model for predicting the thermal transport

ference in the heat transfer coefficient distribution for laminar and turbulent flows. An example of this finding is presented in Fig. 2.2 [48]. It is observed that for turbulent flows, the highest heat transfer coefficients occur around the stagnation region rather than within the stagnation region. Though there is not a complete understanding of why this phenomena occurs, some attribute the change in heat transfer coefficient distribution to the eddy currents and re circulation of flow at the wall that is associated with turbulent flow [54]. As a result, multiple models, including the $k-\omega$ model and the v^2-f model. A comparison of the model to data gathered is presented in Fig. 2.3 [55, 56, 57, 58, 59]. It can be seen that there is great agreement for the downstream conditions, but the accuracy greatly decreases as the flow approaches the stagnation region. Therefore, it is necessary to develop an understanding of the flow conditions within the stagnation region to accurately predict the total heat transfer that occurs within turbulent jet impingement cooling systems.

Research Methodology

When looking at a jet impingement system, there are multiple aspects that need to be dissected to how the experiments were performance. For these experiments, the optical set up used to conduct TDTR must be presented along with the flow loop system used to cool the desired surface.

Time Domain Thermoreflectance

To calculate the heat transfer coefficient in the microchannel, a pump-probe optical technique was implemented to provide the heating to the channel along with measuring the cooling performance. Time domain thermoreflectance, more commonly known as TDTR, is a pump-probe optical technique used to measure the thermal conductivity of thin films [60, 61]. In this experiment, one laser (known as the pump) is used to heat up a region on a thin-film surface while another laser of lower power (known as the probe) has its reflectivity measured through the use of the detector. The pump beam is modified through the use of an electric output modulator (EOM) and the onset of heating from the laser to altered through a delay stage. As the time delay changes, the temperature on the thin film surface will change, which will cause the intensity of the reflection of the probe beam to change due to the temperature dependence of the reflectivity of the thin-film surface.

Figure 2.4 outlines the optical set up utilized to perform TDTR for the presented jet impingement experiments. Both the pump and the probe lasers originated from an Ti:Sapphire (Pulse Frequency = 80.1 MHz, Pulse Width = 140 fs, Central Wavelength = 787 nm). The main beam passes trough an isolator and is directed to a polarizing beam splitter (PBS) through the use of a mirror. The section of the beam that passes through the PBS will be the pump beam. After the PBS, the pump beam will pass through the EOM, where the beam is frequency-modulated at 10 MHz to 100 kHz frequencies. The pump then travels through the delay stage, which is an Au retroflector on

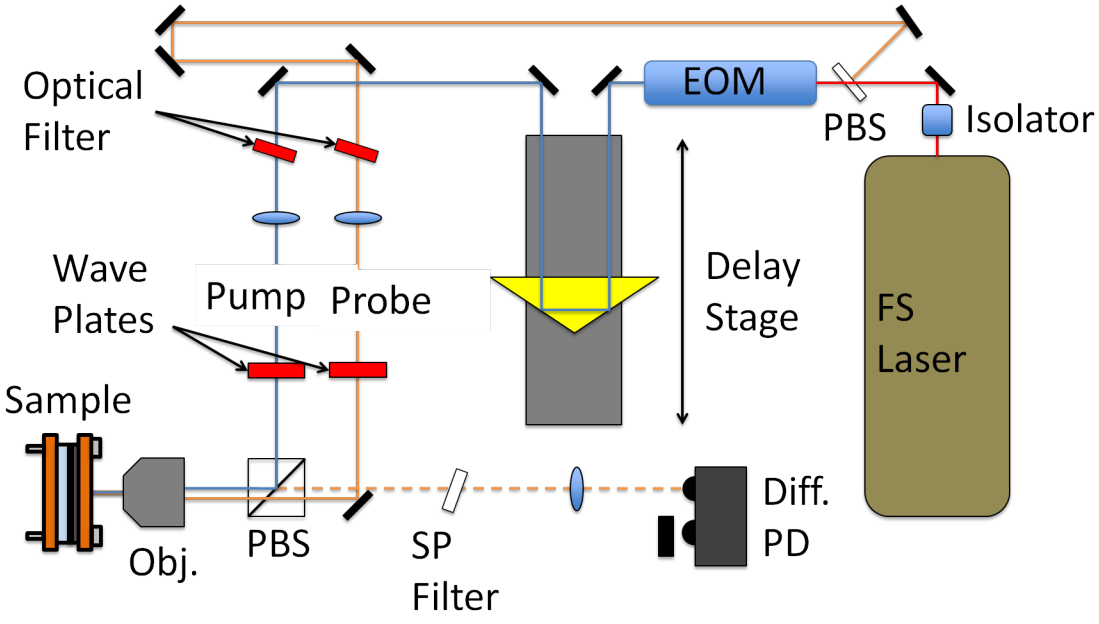

Figure 2.4: A schematic of the optical set up utilized to perform the TDTR experiments to measure the heat transfer coefficients for the jet impingement system.

a computer controlled translation stage. The location of the mirror dictates the distance traveled by the pump beam, which dictates the time delay of heating on the sample. A Raman filter is implemented after the delay stage to increase the pump beam frequency to 800 Hz. To control the power of the beam hitting the sample, a waveplate sample in utilized before the pump reflects off of a second PBS (coated for 800 Hz) directs the pump toward a 20x objective. The objective then focuses the pump onto the sample.

The second beam that is reflected off of the first PBS becomes the probe beam for this experiment. The pump beam bypasses the EOM, delay stage, and Raman filters through the use of mirrors. A 780 nm bandpass filter is implemented for the probe beam before a separate waveplate filter is used to control the power of the probe. A mirror directs the probe toward the second PBS, passes through the beam splitter, then enters the same objective as the pump beam. The probe is then

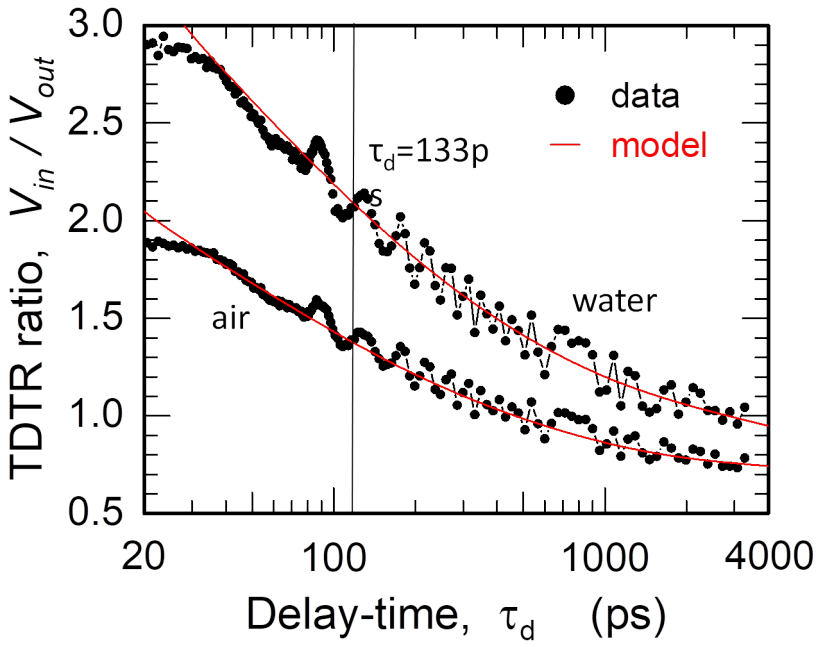

Figure 2.5: TDTR readings for the thin-film Hf-alloy on FS with two different ambient fluids at f_{mod} set to 971 kHz.

focused onto the sample at the same location that the pump beam is focused on.

After hitting the thin-film sample, the reflection of the two beams travel back to the objective on the original path of the other beam. The objective collimates both the beams and the second PBS directs the pump beam reflection away from the detector. Before the reflected probe beam reaches the detector, two filters are used for the beam; one neutral density filter to control the power of the beam approaching the detector and one low pass filter to ensure no residual pump beam reflections interfere with the intensity reading. A detector lens is then used to focus the probe beam into the photodiode detector/sensor to be read. The voltage from the detector then passes through a 971 kHz bandpass filter to a lock-in amplifier via triple shielded RF coax-cables.

The voltage from the detector is divided into two parts by the lock-in amplifier; an in-phase voltage

(V_{in}) and an out-of-phase voltage (V_{out}) in the frequency domain. The ratio of the in-phase voltage to the out-of-phase voltage ($-\frac{V_{in}}{V_{out}}$) is the main measurement to be analyzed in TDTR experiments [60, 61, 44, 62]. Figure 2.5 displays TDTR measurements taken from a Hf-alloy coated fused silica (FS) sample in contact with air and still water in the microchannel with the pump modulation frequency (f_{mod}) set to 971 kHz. For the heat transfer results presented, the TDTR beam travels through the FS and heats the Hf-alloy upon contact, so the thin-film metal acts as both the heater and the surface to be cooled. The experiments were conducted this way so that way the cooling fluids would be in contact with the Hf-allow instead of the FS. The experiments shown in Fig. 2.5 were to conducted to find the thermal conductivity (Λ), thickness (t), and volumetric heat capacity (C_p) since these material properties are related to the changes in the ratio as the delay time changes. For the Hf-alloy on FS displayed in Fig. 2.5, $\Lambda = 0.055$ W/m-K, C_p = 1.86 W/cm^3-K, and t = 130 nm. The oscillations that occur in the ratio values about the model line after 90 ps delay is brought upon because of the Brillouin zone scattering from the heating of the laser in the thin-film metal [12].

The ratio values measured from TDTR experiments at a certain time-delay can be used to calculate the heat transfer coefficient. Based off of Newton's Law of Cooling, which states,

$$h = \frac{q"}{\Delta T} \tag{2.1}$$

where h is the heat transfer coefficient, q" is the heat flux, and ΔT is the temperature difference between the fluid and the plate. The heat flux from the laser can be calculated by using the following equation:

$$q" = \frac{(1-R)\tilde{P}}{\pi w^2} \tag{2.2}$$

where R is the reflectivity of the sample, $\tilde{P}$ is the average power of the pump beam dissipated

into the fluid, and w is the focused beam waist of the pump laser ($w \approx 9.5\mu m$). The temperature difference between the Hf-alloy and the fluid is found through the following equation:

$$\Delta T = \frac{(1-R)\tilde{P}}{\pi w^2}[\frac{1}{e_{th}\sqrt{\omega}}] \tag{2.3}$$

where e_{th} is the thermal effusivity and ω is the AC heating frequency of the modulated pump laser. These two terms are defined by:

$$e_{th} = \sqrt{\Lambda_{eff} C_p} \tag{2.4}$$

$$\omega = 2\pi f_{mod} \tag{2.5}$$

where Λ_{eff} is the effective thermal conductivity. Combining the following equations yields the following relationship to calculate the heat transfer coefficient.

$$h^{\omega} = e_{th}\sqrt{\omega} = \sqrt{2\pi f_{mod} \Lambda_{eff} C_p} \tag{2.6}$$

It should be noted from Fig. 2.5 that the use of different working fluids interacting with the thin film surface yielded different ratio values. This is attributed to the different fluid thermal effusivity. The ratio has also been shown to change when conducting TDTR when the same working fluid is undergoing different conditions (i.e. advenction, boiling) [44]. Since the volumetric heat capacity is a fluid property that does not greatly change under different conditions, the change in the ratio can be associated with the change in the effective thermal conductivity of the fluid. Therefore, obtaining the effective thermal conductivity for the TDTR experiments can be used in Equation 2.6 to find the heat transfer coefficient in the thermal boundary layer. However, this method cannot

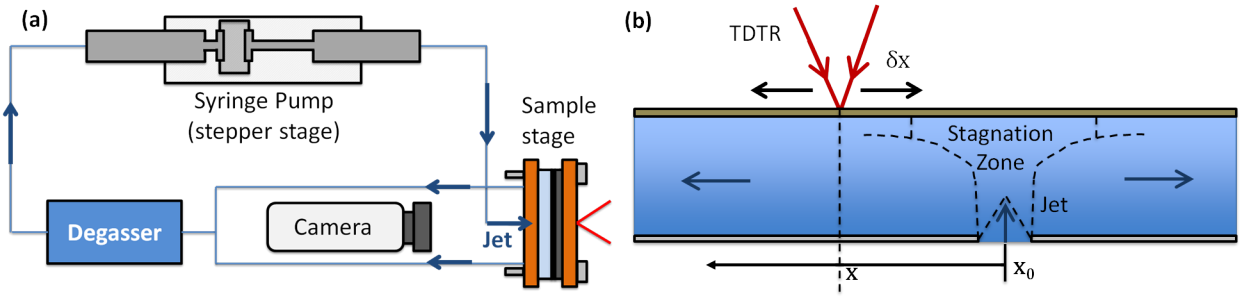

Figure 2.6: (a) The dual syringe pump system implemented to create the jet impingement flow loop system. (b) A schmatic of the jet impingement microchannel and how the TDTR lasers interact with the fluid in the channel.

be used to find the heat transfer coefficient in the bulk motion of the fluid due to the thermal penetration depth of the pump laser. The thermal penetration depth of the pump laser is defined as the distance into the fluid from the thin-film surface at which the heating will be experienced into the fluid. The thermal penetration depth is defined through the following equation [63]:

$$\delta_{tp} = \sqrt{\frac{\Lambda}{\pi C_p f_{mod}}} \tag{2.7}$$

For this study, the thermal penetration depth ranges from 200 to 300 nm. Due to the how thin this region is, TDTR is very sensitive to the hot spot temperature since the fluid within the region can be assumed to be the wall temperature (T_{hs}). Therefore, TDTR can measure the local heat transfer coefficient since the wall temperature will be dictated by the thermal effusivity (through the effective thermal conductivity).

Jet Impingement Flow System

Figure 2.6 (a) reveals a schematic of the jet impingement flow loop system used in this experiment. Within the sample stage, the FS faces toward the TDTR lasers so water and interact and cool the Hf-alloy thin-film being experiencing the heating from the lasers. The channel for water flow was fabricated through laser cutting Teflon (thickness = 1.59 mm) to the specified dimensions (20.5 mm X 1.2 mm). An acrylic piece was placed between the back copper plate and the Teflon channel to guide the fluid flow from the nozzles to the channel. The sample, Teflon channel, and acrylic are sealed by compressing two copper plate around the set up, with the compression brought upon through the use of fasteners. A dual syringe pump system on a computer-controlled stepper motor stage is implemented to create the fluid flow. As the stepper motor stage moves, one syringe pump drives the fluid flow toward the sample and the other syringe collects the fluid after interacting with the sample. The fluid from the driving syringe is pushed toward the sample stage and becomes the impinging jet for the cooling system. Meanwhile, two nozzles are used for the outlets of the cooling channel. These two outlet lines are combined before the fluid passes through a degasser and then to the collecting syringe. A CCD flea camera (1280 X 1024 Resolution) is used to ensure the pump and the probe beam are focused within the microchannel.

Further details of the interactions with the TDTR lasers and the microchannel are provided in Fig. 2.6 (b). The center of the stagnation zone is what is determined as the initial x position (x_0). The sample stage is placed on a stepper motor stage while the position of the TDTR lasers are fixed. Therefore, as the sample moves with the translation stage, a different x location in the microchannel interacts with the TDTR lasers, meaning the heat transfer coefficients can be measured at different x locations in the microchannel. This set up is implemented to measure the heat transfer coefficient within the stagnation region and at downstream conditions at different Reynolds numbers.

Findings

For the hot spot jet impingement results, an experiments was conducted where the pump beam used for TDTR measurements heats up a sample in a microchannel. The pump and probe laser powers were set to 7.5 mW and 4.0 mW, respectively. These laser powers provide the heating to the channel while avoiding additional dc heating of the microchannel wall, which would increase the wall temperature beyond what is required for nucleation. The time delay between the pump and the probe was set to 133 ps and f_{mod} was set to 971 kHz. This time delay was chosen based off of the findings in Fig 2.5, where the data matches well with the model while the Brillouin Zone scattering is occuring. For these experiments, two variables were changed; the Reynolds number of jet and the x location of heating and measurement. The two locations focused on for this investigation was the stagnation point (x_0) and a downstream condition (x = 2.02 mm). The Reynolds number varied from zero (stagnation condition) to 6432. For this experiment, the H/d value was constant at 2.31. This experiment was performed to shine light on the ability of utilizing TDTR to develop a heat transfer coefficient map within a microchannel through the use of TDTR [64].

Figure 2.7 (a) displays the thermal effusivity results of the jet impingement experiments measured with TDTR. It should be noted that two different behaviors were exhibited for the two different conditions. With the stagnation point, the thermal effusivity remained relatively constant at different Reynolds number ouside of Re = 5400. This reveals that the temperature at the wall and within the thermal boundary layer remains relatively constant throughout all of the flow conditions. Therefore, the measured thermal effusivity does not change even as the Reynolds number is increased. Due to this result, it can be established that greater heating from the TDTR lasers or another heating source can be increased for using this thin-film Hf-alloy to observe if any changes will occur with the heat transfer coefficient with turbulent flow-fields. For Re = 5400, the deviation

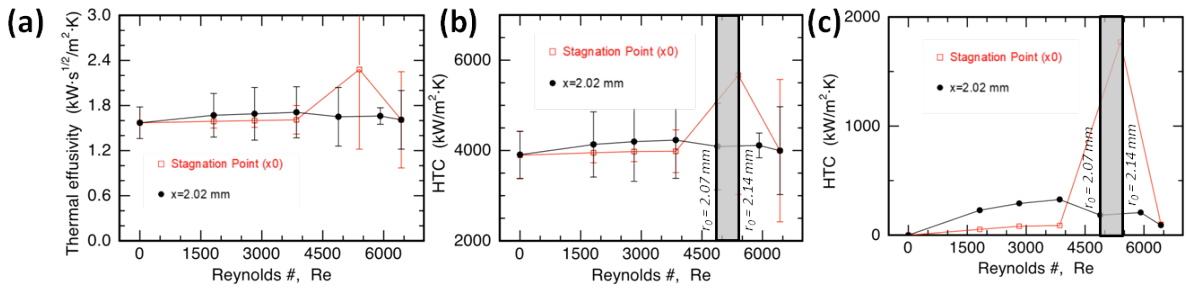

Figure 2.7: (a) The thermal effusivity as a function of the Reynolds number at the two different locations. (b) The heat transfer coefficient as a function the Reynolds number at the two different locations. (c) The added heat transfer coefficient by the jet as a function of the Reynolds number at the two different locations. The shaded regions in (b) and (c) correspond to the measured anomaly with the corresponding r_0 at those Reynolds numbers.

from the constant value could be the result of turblent mixing occur within the channel under that certain condition or due to laser misalignment.

However, a different trend is observed for the downstream condition. It can be seen that for Reynolds numbers up to roughly 4000 that as the Reynolds number increases, the thermal effusivity also increases. However, after Re = 4000, the thermal effusivity quickly decreases to close to the stagnation condition. This phenomenon could be explain due to the growth of the stagnation region with the increasing Reynolds number, which is an occurrence that has already been reported by Chen et al. [65]. Another study conducted by Lienhard concluded that a transition in the heat transfer of a jet impingement system occurs when the boundary layers reaches the film thickness of the cooling fluid. This transition occurs at a certain distance, r_0, which can be found through the following relationship [66].

$$r_0 = 0.1773 Re_d^{1/3} d \tag{2.8}$$

where d is the diameter of the jet. Based on Equation 2.8 and the diameter of the jet, r_0 for Re = 4885 is 2.07 mm. This distance also corresponds to the change in cooling behavior experienced

in the downstream condition. This distance along with the stagnation region width at Re = 5400 ($r_0 \approx 2.14$ mm) is presented in Fig. 2.7 (b) and (c). This reveals the significance of utilizing TDTR to measure the heat transfer coefficient being sensitive to the stagnation region growth at differing Reynolds numbers.

Figure 2.7 (b) displays the heat transfer coefficient values measured with the jet impingement cooling system. This was accomplished by using Equation 2.6 with the thermal effusivity values provided in Fig. 2.7 (a). Since the heat transfer coefficient is directly proportional to the thermal effusivity, the same trends discussed with the thermal effusivity will be seen in the heat transfer coefficient. It is important to note that since the thermal penetration depth of the TDTR lasers is roughly 250 nm, the heat transfer coefficients displayed are the heat transfer coefficients in the short length scale (or high frequency). However, the heat transfer coefficient values displayed is the total heat transfer coefficients, as noted that the heat transfer coefficient at the stagnant condition. In order to find the cooling enhancement contribution through the introduction of the jet impingement, the heat transfer coefficient value at the stagnant condition is subtracted from the values measured at higher Reynolds numbers. This method of measuring the enhanced heat transfer coefficient ($h_{\uparrow}$) is summarized in the following equation.

$$h_{\uparrow} = h - h_0 \tag{2.9}$$

where h is the measured heat transfer coefficient and h_0 is the heat transfer coefficient at the stagnant condition. The values of $h_{\uparrow}$ are displayed in Fig. 2.7 (c). These results reveal that the jet impingement cooling does provide enhanced cooling in both the stagnation region and the downstream conditions, even though the enhanced cooling is more evident in the downstream condition. These results show the reliability in using TDTR to capture thermal transport behaviors near a heated wall. This provides a good experimental protocol when discussing the results in the next

chapters, where TDTR can be utilized to capture different near wall behaviors for different wetting characteristics and chemistries.

CHAPTER 3: SURFACE WETTING

Literature Review

Another aspect of research that has taken interest in the heat transfer community is how a fluid wets a surface [67, 68]. Surface wetting refers to the behavior of a fluid on the surface, namely how it moves and rests on a surface. In previous studies of surface wetting, the equilibrium contact angle of a resting droplet on a surface has been desired to define the surface wettability [69, 70, 71]. For instance, the equilibrium angle of water determines an important characteristic of a surface, whether it is hydrophilic ($\theta_{eq} < 90°$) or hydrophobic ($\theta_{eq} > 90°$) [72]. The equilibrium angle is brought upon by an energy balance between the three interfacial energies at the triple contact line. This definition gives rise to Young's Equation, which is found through conducting an energy balance [73].

$$\cos\theta_{eq} = \frac{\gamma_{sv} - \gamma_{sl}}{\gamma_{lv}} \tag{3.1}$$

where γ_{sv}, γ_{sl}, and γ_{lv} are the solid-vapor, solid-liquid, and liquid-vapor interfacial energy, respectively.

One of the key reasons why the study of surface wetting is of interest to the thermal community is due to the rewetting action that occurs as a fluid begins to nucleate on a heated surface. This movement of fluid over the nucleation site creates an increased heat removal rate for two phase systems compared to single phase systems. For reference, when looking at the heat transfer coefficient values captured in Table 1.1, it can be seen that for all cooling techniques that two-phase flows yield higher thermal transport than single-phase flows. Therefore, multiple efforts have been investigated to increase the wettability of a surface to increase the critical heat flux that a surface can experience [72, 68, 74]. For instance, efforts have been made to alter the physical surface

conditions (i.e. surface roughness, patterned surfaces) and chemical surface conditions (i.e. hydrophobic and hydrophilic surfaces) to detect how different surface conditions affect the surface wetting [75, 41, 76, 77, 78].

When analyzing wetting with nano- and microstructures, there are three main states that the types of wetting can be divided to; Cassie-Baxter, Wenzel, and hemiwicking. The Cassie-Baxter state describes the phenomenon where a droplet will rest on top of structures on a surface [79, 80]. There are several instances in nature that exhibit a Cassie-Baxter state for drying purposes, such as Lotus leaves and butterfly wings [79]. The Wenzel state refers to when a droplet does enter the wetting structure, but instead of spreading throughout the entire array, the droplet maintains its spherical shape and does not move. Different research has been conducted over the past few decades about the transition from Cassie-Baxter to Wenzel State and how to encourage wetting during the transition [81, 82, 83]. It should be noted that Cassie-Baxter and Wenzel states occur when the substrate surface is hydrophobic [81]. Hemiwicking, on the other hand, is the phenomenon which occurs when the substrate surface is hydrophilic. Hemwicking is the capillary action that occurs on a structured surfaces where the capillary forces draw the fluid across the surface [43]. In a sense, the structures on the surface act like a fluid pump on the surface without any moving parts.

Hemiwicking

For the purpose of this dissertation, current models and understandings of hemiwicking are going to be presented since, in light of heat transfer and heat transfer applications, hemwicking is the most relevant of the different wetting states. It has been exhibited before that heated surfaces can experience a higher critical heat flux when hemiwicking occurs on the surface [84, 43, 39]. As a result, investigations have been done by differing research groups in the field of heat transfer and thermofluids [84, 85]. Along with gaining interest in academia, utilizing wicking structures

on thermal transport devices, such as heat pipes, have also risen in popularity. On heat pipes, the wicking structures draw the fluid from the condensed region (i.e. cooling region) back to the evaporating region (i.e. heated region), essentially creating a pump for the working fluid without any moving parts [85, 40].

Part of the ongoing research that has been going on with hemwicking has been being able to predict the velocity at which a fluid will travel through a pillar array with a given pillar geometry. One common parameter that is used to define the wicking geometry is the surface roughness, which is defined as the ratio of the total surface area to the projected surface area (the surface roughness is commonly denoted as f) [86]. Based on the surface roughness, different hemiwicking models have been derived. This is commonly accomplished through performing a force balance between the driving force (i.e. capillary force) to the resisting force (i.e. viscous force). Based off of the force balance, the following scale is derived

$$U \sim \frac{\gamma}{\mu}\frac{\eta H}{L} \tag{3.2}$$

where μ is the dynamic viscosity of the fluid, H is the height of the pillars, L is the distance the fluid has traveled in the array, and η is a dimensionless coefficient from the wicking geometry, which is defined through the following equaiton [86]:

$$\eta = \frac{(s_y - d)(f-1)}{(s_y - d) + H(f-1)} \tag{3.3}$$

where s_x and s_y are the pillar spacing in the x- and y-directions, respectively, and d is the diameter of the pillar. However, Krishnan et al. has recently attempted to derive a model that incorporates the interfacial interactions that occurs within the evaporating fluid meniscus through the extension

of an evaporating fluid meniscus from the last pillars in the array (x_0). Based on experiments that were conducted, the liquid-surface factor is introduced through the following equation [87].

$$S = \frac{Hs_x(s_y - d)\sqrt{f-1}}{Lx_0^2} \tag{3.4}$$

Based off of this updated surface factor and dynamics that are already known regarding hemiwicking, Krishnan et al. establishes the following two model lines for wicking velocity from a reservoir and from droplet, respectively [87].

$$U = \frac{S}{95\pi}\frac{\gamma}{\mu} \tag{3.5}$$

$$U = \frac{S}{95}\frac{\gamma}{\mu} \tag{3.6}$$

It should be noted that the factor of π is brought upon by the LaPlace pressure of the droplet on the surface as compared to the reservoir.

Soft Surface Wetting

Another aspect of surface wetting that has increased in popularity over the past decades has been the wetting interactions of a fluid on a soft surface. Understanding how a fluid interacts with a soft surface is important to understand in the fields of soft tissues, polymer gels, and inkjet printing [88, 89, 90]. The underlying assumptions of the previously mentioned Young's Equation (see Equation 3.1) is that the surface is flat and will not deform due to the presence of the droplet [73]. However, it has been discovered that the surface tension of a fluid on a soft surface will

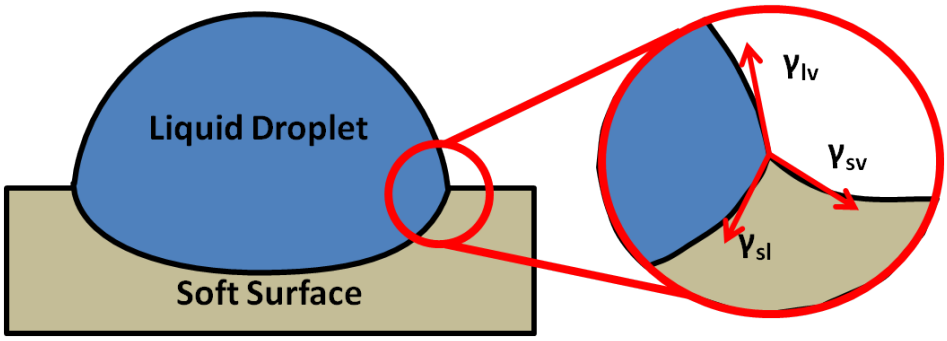

Figure 3.1: An example of how the interfacial energies affect the soft surface and create the microscale deformations.

lead to noticeable deformations on the surface [91, 92, 93, 94, 95, 96]. For instance, micron scale deformations can occur on for surfaces that have a Young's Modulus below 10 kPa when water begins to evaporate off of the surface [97]. Figure 3.1 provides an illustration of the interfacial energies and how the deformations occur on the soft surface. Since it has been shown that vertical deformations do occur on soft surfaces, Young's Equation is not an accurate wetting model to use when describing soft surface wetting [97, 98].

As a result of these findings, investigation have been performed by various research groups to accurately describe the wetting behavior of different fluids on soft substrate under different conditions. For instance, the scale at which the soft surface will deform under different fluid surface situations have been investigated. There are two main components of the fluid dynamics on the surface that contribute to the deformations of the surface; the interfacial energies and the LaPlace Pressure [99]. The contribution of the interfacial energy to the deformation begins with the vertical component of the liquid-vapor interface. Assuming an initially flat surface to begin with, the vertical force from the interface is the following equation.

$$F_{vert} = \gamma_{lv} \sin \theta_{eq} \tag{3.7}$$

For rigid materials ($G \sim 100GPa$), the stiffness is so great that the deformation that occurs only happens on the molecular level and does not affect the overall surface wetting [99]. However, as the stiffness of the substrate decreases, the deformations go from the molecular length scale to the micron length scale [97, 93]. Different attempts have been made to scale the deformation that occurs on the surface from both an analytical and empirical approach [100, 101, 97, 102]. These investigations have revealed some scalings for the deformations that occur due to the presence of the droplet. First, for the horizontal component of deformation, it has become accepted that the deformation scales as the following [93, 98].

$$\delta_{horizontal} \sim \frac{\Upsilon_s}{E} \tag{3.8}$$

where Υ_s is the solid surface tension. This region is defined as the horizontal distance along the surface where non linear deformations will occur due to the presence of the fluid [93]. Meanwhile, the vertical deformations that occur on the surface is scaled as [103, 104]:

$$\delta_{vert} \sim \frac{\gamma}{G} \sim \frac{2\gamma(1-\varepsilon)}{E} \tag{3.9}$$

where δ_{Vert} is the deformation on the surface, G is the shear modulus of the surface, and ε is the Poisson's Ratio. Along with the deformations that occur due to the interfacial energies, the LaPlace Pressure has also been found to lead to the deformation of the surface. The LaPlace Pressure is equated as [105]:

$$\Delta P_{LaPlace} = \frac{2\gamma}{R} \tag{3.10}$$

where $\Delta P_{LaPlace}$ is pressure difference between the outside and the inside of the droplet and R is the radius of the droplet. The LaPlace pressure is already an important aspect of characterizing droplets as it has been known to drive droplet spreading and shaping [106, 107, 108]. With the recent

discoveries of the surface deformations on soft materials, investigations have been performed to discover the role of the LaPlace pressure in the deformation of the surface [99, 109]. When looking at the LaPlace Pressure and the scales of deformation found in previous works, the surface tension plays a dominant role in how much deformation a soft surface will experience.

Recent studies have also exhibited deformations of micro- and nano structures on surfaces as a working fluid evaporates from the structures [110, 103]. However, even though multiple studies have shown this phenomena, there are disagreements to the main agent behind the deformation of the structures [111]. Namely, there are two forces that most contribute to the observed deformations; the LaPlace pressure associated with the evaporating meniscus from the top of the structures and the capillary forces that draw the fluid to the structures. The equation for the capillary energy found in pillars is defined through the following equation [111]:

$$W = -2\pi\gamma R^2 \cos^2\theta \ln\left(\frac{l_c}{s+\sqrt{s^2-4R^2}}\right) \tag{3.11}$$

where s is the pillar spacing and l_c is the capillary length, which is defined through the following equation.

$$l_c = \sqrt{\frac{\gamma}{\rho g}} \tag{3.12}$$

Based off of the energy provided in Equation 3.11, the torque the structures experience can be calculated.

$$\tau_c = \frac{\pi\gamma R^2 h \cos^2\theta}{\sqrt{(s/2)^2 - R^2}} \tag{3.13}$$

Meanwhile, the torque associated with the LaPlace pressure is found through the following equation.

$$\tau_l \approx \frac{2R\gamma\cos\theta}{\frac{s}{2}-R}\int(h)dh = \frac{\gamma R h^2\cos\theta}{\frac{s}{2}-R} \tag{3.14}$$

From the two aforementioned equations, a ratio of the LaPlace torque to the capillary torque can be derived.

$$\frac{\tau_l}{\tau_c} \approx \frac{h}{\pi R\cos\theta}\sqrt{\frac{\frac{s}{2}+R}{\frac{s}{2}-R}} \tag{3.15}$$

Based off of these equations, several inferences can be made regarding the dominating force on the pillar structures, namely that the capillary force is generally much greater than the capillary torque. Therefore, the critical Youngs Modulus before deformation is based on the LaPlace force between the pillars as the thin film meniscus changes. The critical Youngs Modulus is then defined as [111]:

$$E_{crit} = \frac{32\sqrt{2}\gamma\cos^2\theta h^3}{3d^4}f(r) \tag{3.16}$$

where $f(r)$ is a function based on the ratio of the distance between pillars to the diameter of the pillars.

Inertial Versus Viscous Wetting

Along with the research performed for sessile droplets on a surface, different investigations have been performed to find how different fluids wet on a surface [112]. When a droplet wets a surface, the surface tension of the fluid is the main driver of the fluid. As the fluid wets the surface, the angle noticed will be different than the equilibrium contact angle the fluid takes when the droplet is at rest. Therefore, the driving force of a droplet wetting a surface can be expressed through the following equation [92, 99].

$$F_{drop} \sim (\cos\theta - \cos\theta_{eq}) \tag{3.17}$$

where θ is the advancing angle of the fluid at a particular moment. Once the advancing angle of the fluid reaches the equilibrium angle of the fluid, the driving wetting force reduces to zero and the wetting motion of the fluid stops. Even with this driving force known, it is desirable to scale the droplet wetting in terms of fluid properties to better predict how any droplet will wet a surface. When looking at how a droplet wets a surface, there are two main types of wetting that occur that are governed by different dynamics; inertial wetting and viscous wetting [92, 113]. Inertial wetting is the first stage of wetting and typically only lasts a few milliseconds [114, 115]. Various research groups have conducted experiments in an attempt to discover the main physics behind the inertial wetting region. The time scale at which the droplet moves has been accepted by most of the research groups and can be described through the following equation [115, 114, 113, 92].

$$\tau_{inert} \sim \sqrt{\frac{\rho R^3}{\gamma}} \tag{3.18}$$

Chen et al. [92] discovered an interesting result when performing wetting experiments on soft surfaces of different natural wettabilities (i.e. varying contact angles). This set of experiments that discovered that the only factor that changed the inertial wetting dynamics on the different surfaces was the natural wettability and that the soft materials did not impede upon the wetting

dynamics in the inertial regime. However, the softness of the materials still played a significant role in the amount of time the inertial forces dominated the droplet spreading. It was found that inertial wetting dynamics last longer on surfaces that are less stiff (i.e. lower shear modulus).

The second regime of wetting is known as viscous wetting, which follows right after the inertial wetting regime and has different physics driving the fluid. Similar to the inertial regime, extensive experiments have been conducted in an attempt to characterize the wetting velocity in the viscous regime [94, 92, 77]. Within the viscous regime, Tanner's Law is commonly used to characterize the droplet spreading [114]. Tanner's Law is expressed through the following equation.

$$\frac{r}{R} \sim (\frac{\gamma t}{\mu R})^{1/10} \tag{3.19}$$

where r is the distance from the contact point the fluid travels and μ is the dynamic viscosity of the fluid. Tanner's Law can be obtained through performing a force balance between the capillary forces and the viscous forces [92, 94]. When comparing the time scales in the inertial regime (see Equation 3.18) and the viscous regime (see Equation 3.19), there are a few differences in the wetting dynamics and different properties drive the motion of the fluid. The main difference that can be inferred are the fluid properties that dictate the scale. While the inertial time scale is based around the ratio of the density of the fluid to its surface tension, the viscous time scale is dictated by the ratio of the surface tension to its dynamic viscosity. This difference in the time scale reveals that when analyzing how a droplet spreads on a surface, that one needs to be aware of the two different regimes in order to accurately predict the wetting behaviors.

Another area of interest with the dynamics of fluid spreading on soft surfaces is the presence of a "soft ridge" to moves along with the triple contact line. With the presence of a ridge the forms of a sessile droplet, it was desirable to see if the same ridge could be captured with a moving droplet. Even though in the past it has been difficult to visually capture this ridge as a fluid wets across the

surface, recent experiments have been able to capture the wetting ridges of a wetting droplet as it diffuses across the surface [97, 116, 117]. One of the findings detected with the enhancement in visualization has been a "stick-slip" motion that occurs on the soft surfaces [102, 117, 118]. The "stick-slip" motion refers to when at lower wetting speeds, the ridge cause by the presence of the fluid will cause the fluid to "stick" to a position. As the fluid builds, the contact angle will continue to change up until there is enough interfacial energy to push the fluid forward on the sample. This gives a "slipping" motion where the triple contact line will move and eventually be pinned again where the motion process will be continued [102]. Another important characteristics of soft surface wetting is viscoelastic braking. Viscoelastic braking is the slowing down of a fluid on a soft surface due to the deformations that are occurring on the soft surface [116]. Various different research groups have discovered this effect under different wetting circumstances [119, 120]. Between this different theories of the impact of surface wetting on soft surfaces, there is great interest to fully understand the full impact of the droplet dynamics on soft surfaces.

Research Methodology

For this chapter, a unique method to fabricate microstructured samples is introduced for both soft surface wetting experiments along with general surface wetting experiments. Soft surface wetting experiments were conducted to see the effect the Youngs Modulus of a sample has on the hemiwicking. Along with analyzing the physical surface conditions, the surface chemistry is analyzed through applying a polyvinyl alcohol (PVA) self-assembled monolayer (SAM) to different thin-film, microstructured surfaces.

Soft Surface Wetting

For the soft surface wetting experiments, an in-house stamping apparatus was created to create PDMS hemiwicking samples in both a time and cost effective method [121]. After the PDMS samples were made, two main experiments were implemented to characterize the wetting characteristics on soft materials. Vertical hemiwicking from a reservoir experiments were conducted to investigate the impact the stiffness of soft materials has on hemiwicking performance. Meanwhile, droplet wetting experiments were conducted to observe any changes in the inertial wetting characteristics on soft materials.

Sample Fabrication

With the rise of hemiwicking in recent research, different methods have risen in ways to fabricate the micro and nano sized structures. One of the more popular methods that have risen is thermal imprint lithography, where the desired layout is stamped through heating a desired layout and removing the mold to create the structures [122, 123, 124]. However, this process has an inherent sensitivity to the temperature used to create the structures along with the use of multiple coatings throughout the process to ensure the accuracy of the wicking structures [125]. This issue coupled with the impracticality of using this method for macro-scale applications reveals that utilizing lithography is not the most ideal method from a expediency and cost stand point. There are methods for large scale printing of micro structures, such as spin or dip coating, but there is a random nature to these procedures that may not be ideal for different wetting application [126].

Therefore, a new method was created to fabricate hemiwicking samples in both a time and cost effective manner. This method is a negative mold casting method where a mold is created with an in-house stamping apparatus. A schematic of the stamping apparatus created is presented in

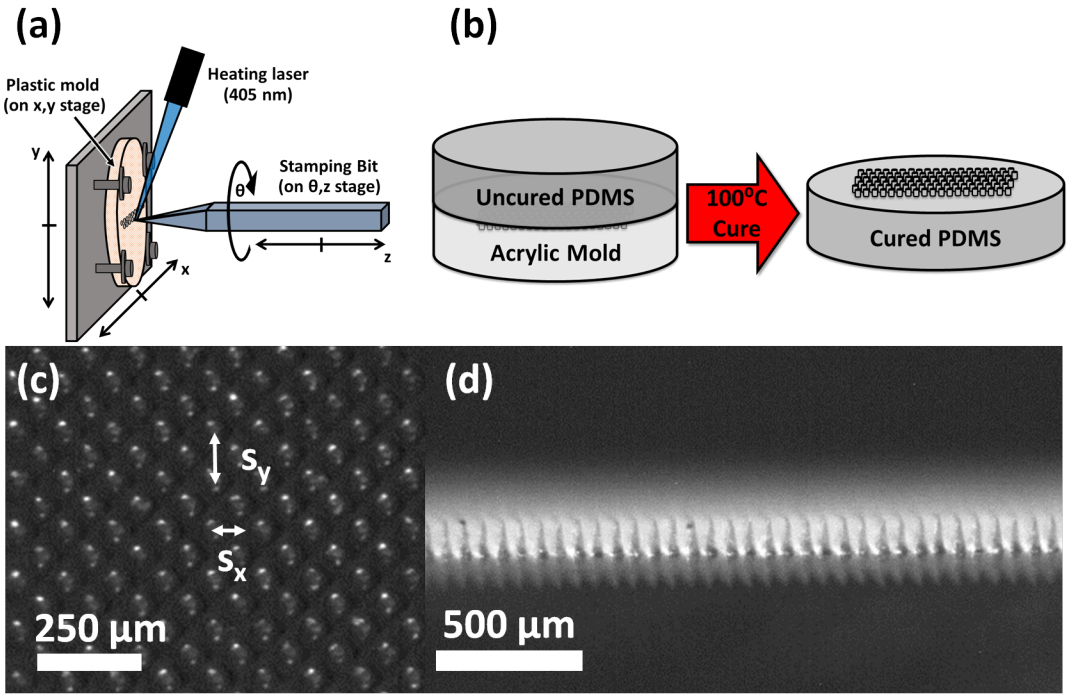

Figure 3.2: (a) A schematic of the stamping apparatus created to fabricate the plastic negative molds for the hemiwicking samples. (b) The procedure taken to create the PDMS samples after the plastic mold has been created. (c) A top view of Sample 2, which was created for the soft material hemiwicking experiments. The pillar spacing definitions, S_x, S_y are also provided. (d) A side view of Sample 2 created for the soft material hemiwicking experiments.

Fig. 3.2 (a). This instrument consists of two sets of stepper motors; one set to control the x- and y- location of the plastic mold and another set to control the z- and θ- positions of the microdrill bit. A computer program reads a user created bitmap to control the locations of the plastic mold (i.e. the pillar spacing) and the micro drillbit (i.e. the pillar height). The diameter of the pillars is determined by the diameter of the microdrill bit used. A heating laser (P = 3W, λ = 405 nm) is implemented to heat up the microdrill bit during the process to assist in the cavity fabrication.

After the mold was created, the PDMS samples could be created. Fig. 3.2 (b) displays the process taken to create the PDMS samples with the negative mold created with the stamping apparatus.

The ratios of the monomer to cross linker along with the curing time for each sample varied to change the Young's Modulus of each sample [98]. The uncured mixture between the monomer and cross linker is poured over the plastic mold in a sample holder, where the uncured PDMS will fill in the cavities which become the wicking structures. The uncured PDMS is then placed in an evacuated chamber to remove any air pockets from the sample which could affect the stiffness and structural integrity of the sample. After the removal of the air pockets, the sample is heated at 100 °C to cure the sample. Figure 3.2 (c) and (d) shows pictures of one of the samples used in this study from two different angles after the aforementioned process.

To characterize the stiffness of each of the samples, a cantilevered beam experiment was used to calculate the Young's Modulus of each sample. To perform this experiment, one end of sample was clamped to a fixed position while the other ended was subjected to a force brought upon by placing a weight at the end of the sample. Weights of 0.2, 0.5, 1, 2, and 5 g were placed on the sample to measure the deflection at different forces. The deflection of the sample was captured through the use of a CCD Flea Camera. With the geometry of the sample known and the deflection of the sample measured, the following equation can be used to find the Young's Modulus.

$$E = \frac{4L^3F}{bh^3\delta} \tag{3.20}$$

where E is the Young's Modulus, L is the length of the sample, F is the force the sample is subjected to, b is the width of the cross section, h is the height of the sample, and δ is the deflection with the given force. Table 3.1 displays the wicking geometries and the stiffnesses of the samples used in this study.

To develop a full understanding of soft material stiffness on the wetting properties of a fluid, two experiments were conducted to capture the hemiwicking performance and the inertial wetting performance. The working fluids used in this study were ethanol (ρ_{eth} = 789 kg/m^3, γ_{eth} = 0.02197

Table 3.1: The Wicking Geometry and Stiffnesses of the PDMS Samples.

Sample	S_x (μm)	S_y (μm)	H (μm)	d (μm)	E (MPa)
1	61.6	127.0	120.6	59.0	1.21 ± 0.0910
2	58.4	124.6	123.2	53.1	1.16 ± 0.0854
3	60.3	125.8	160.34	51.3	0.388 ± 0.134
4	60.8	129.6	120.0	59.2	1.95 ± 0.188
5	62.5	126.4	121.1	53.8	0.337 ± 0.0443
6	58.2	124.0	123.0	51.5	1.98 ± 0.311

N/m, μ_{eth} = 0.001074 Pa-s), isopropyl alcohol (ρ_{isop} = 786 kg/m^3, γ_{isop} = 0.02093 N/m, μ_{isop} = 0.002038 Pa-s), and isooctane (ρ_{iso} = 690 kg/m^3, γ_{iso} = 0.0186 N/m, μ_{iso} = 0.0004784 Pa-s). A vertical wicking from a reservoir experiment was conducted to characterize the impact of hemiwicking while high speed videos of fluid droplets coming into contact with a soft surface were captured to find the changes in the inertial wetting characteristics.

Hemiwicking Experimentation

Figure 3.3 (a) provides a schematic of the vertical wetting experiments conducted with the different working fluids. The soft material surfaces were placed in a fixed position while a reservoir of the different working fluids were placed on a vertical translation stage. The reservoir was raised to the sample until the fluid comes into contact with the wicking array. Once the working fluid comes into contact with the wicking structures, the capillary forces from the structures draws the fluid from the reservoir through the array. An example of the working fluid being drawn from the reservoir is displayed in Fig. 3.3 (b). The motion of the fluid was captured through the use of a Point Grey Flea Camera (Resolution = 4.14 μm/pixel, Frame Rate = 50 fps) and a Phantom v. 12.1 High Speed Camera (Resolution = 13.81 μm/pixel, Frame Rate = 100 fps) . From the videos gathered from these experiments, the wicking velocity and diffusion of the fluid throughout the wicking array can

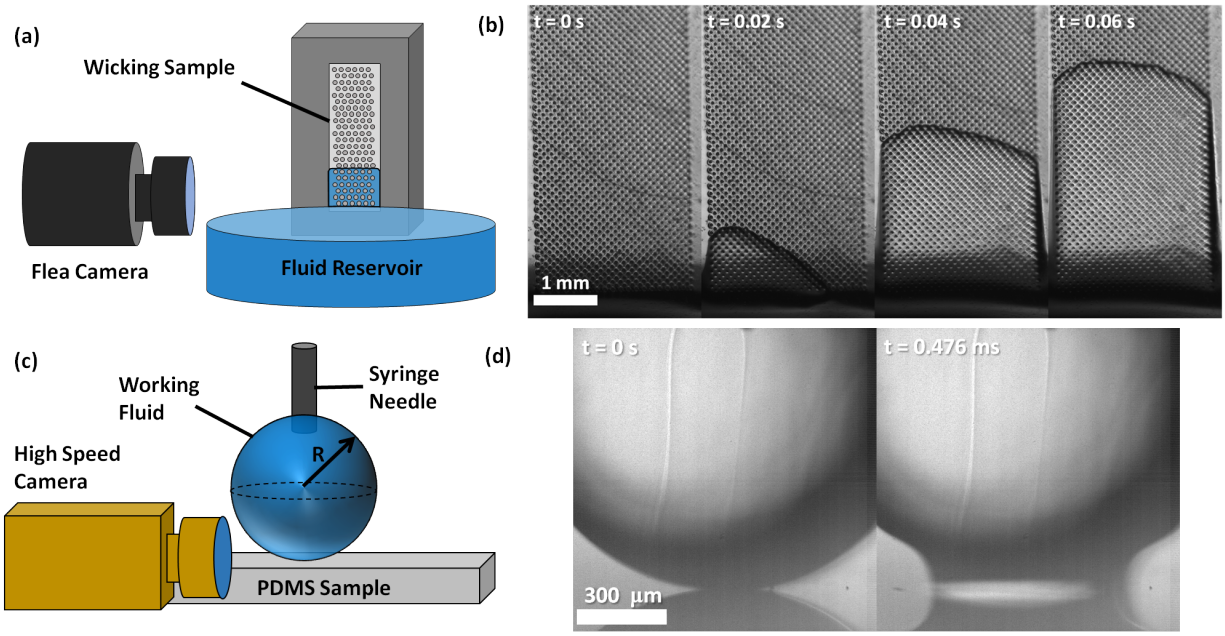

Figure 3.3: (a) A schematic of the vertical wicking experiments conducted to characterize the hemiwicking characteristics (i.e. wicking velocity, diffusion) for the soft materials. (b) Video snapshots of isooctane wicking through the wicking array on Sample 2. (c) A pictorial representation of the droplet experiments conducted to characterize the inertial wetting properties of the different wetting fluids on the soft surfaces. (d) Snapshots of an isopropyl alcohol droplet wetting the surface of Sample 2.

be measured, providing insight to how soft materials can affect hemiwicking performance.

Initial Hemiwicking Velocity

To capture the initial hemwicking velocity, a Phantom v. 12.1 high speed camera (Frame rate = 11001 fps, Resolution = 0.847 μm/pixel) was used to capture the motion of the fluid through the first row of pillars in the microstructured array. An example of the motion across the first pillars in a hemiwicking array is presented in Fig. 3.4. Similar to the full hemiwicking experiments, ethanol, isopropyl alcohol, and isooctane was used as the working fluid for this data. For the

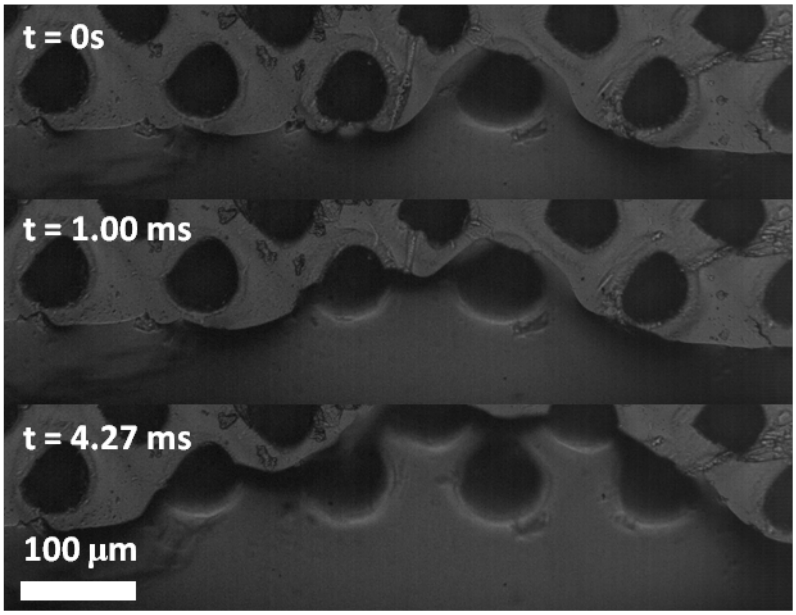

Figure 3.4: A progression of ethnaol traveling across the first row in the microstructured array of Sample 1 (E = 1.21 MPa)

initial hemiwicking velocity, two means of measuring the initial velocity were taken; the maximum measured velocity across the first row in the array and the average velocity across the same location. This was performed since at the frame rate captured, the velocity changes between pillars as the capillary force draws the fluid from one location to the next.

Inertial Wetting Experiments

A simple diagram of the experimental set up implemented to find the inertial wetting characteristics of the different fluids on the soft surfaces is displayed in Fig. 3.3 (c). A fluid droplet is formed manually through the use of a syringe and a gauge 31 needle. The droplet is allowed to increase in volume until the droplet came into contact with the surface, where the droplet will begin to wet the surface. This is done so the velocity of the droplet coming into contact is roughly zero (i.e.

We ≈ 0), meaning there would be no kinetic energy influencing the wetting of the droplet. The wetting action was captured through the use of a Phantom v. 12.1 high speed camera (Resolution = 2.067 μm/pixel, Frame Rate = 21005 fps). Different frames of the droplet spreading on the PDMS surface is shown on Fig. 3.3 (d).

Initial PVA Monolayer Coatings

Applying a PVA monolayer onto hemiwicking samples was utilized to characterize how changing the surface chemistry can affect the wicking behavior of the fluid. By changing the surface chemistry and changing the interfacial interactions at the triple contact line, the wetting behavior will also change, leading to a change in hemiwicking performance (see Equation 3.1). The negative mold method previously mentioned was used to create the base PDMS samples for the wicking structures. Unlike the samples created for the soft wetting experiments, different wicking arrays were implemented for this study. However, rather than have the wicking occur on the PDMS surface, thin-film metal layers were deposited onto the PDMS to have the working fluids wick on different metals (i.e. different initial surface energies). The deposition was performed through DC electron magnetron sputtering with Argon gas. The metals that were deposited on the PDMS samples were aluminum and gold, with titanium needing to be deposited before the gold to act as buffer for better adhesion between the PDMS and the gold. The characteristics of the different samples are provided in Table 3.2.

After the metal has been deposited on the samples, each of the samples were place in an aqueous solution of PVA (10 mg/mL). The samples were treated in the aqueous solution of PVA for 24 hours to create the PVA monolayer on the samples. This procedure has been outlined in Fig. 3.5. After the monolayer has been formed, each samples was subjected to wicking experiments by placing large enough droplets ($V_{drop} \approx 5\mu L$) to allow for wicking throughout the sample without having

Table 3.2: The Wicking Geometry and Metals Used for the Polyvinyl Alcohol Monolayer Experiments

Sample	Material	S_x (μm)	S_y (μm)	H (μm)	d (μm)
A	Aluminum	59.0	117.9	49.4	49.9
B	Aluminum	75.3	153.5	81.7	88.8
C	Aluminum	76.3	150.9	82.5	70.8
D	Aluminum	72.2	149.8	83.0	92.0
E	Aluminum	74.8	143.3	76.5	73.8
F	Gold	114.4	229.2	105.4	108.6
G	Gold	113.6	230.2	100.3	91.8
H	Gold	129.2	253.4	96.4	89.8
I	Gold	126.0	259.0	92.9	52.4

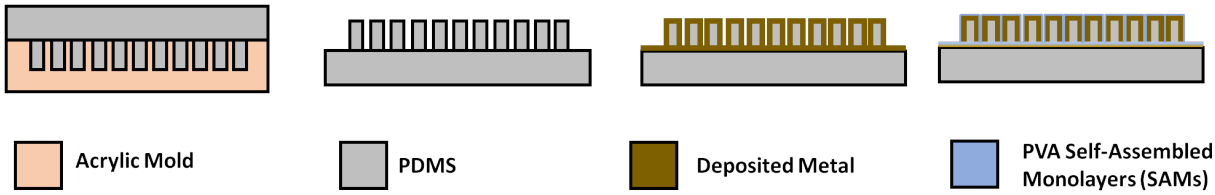

Figure 3.5: The procedure of creating the samples after the stamping apparatus, including the deposition process and the application of the PVA SAM

flooding occur on the sample. The droplet was created through the use of a computer-controlled syringe. For this dissertation, the state of the sample immediately after monolayer formation will be referred to as State 1. The wicking experiments were conducted again 24 hours after removal from the aqueous solution, where degradation of the monolayer (and therefore wicking performance) was observed. The state of the sample 24 hours after monolayer formation will be referred to as State 2. For each trail, two camera were utilized to capture the changes in the wetting characteristics, an overhead camera to capture changes in the meniscus extension and a side camera to capture the hemiwicking velocity.

Findings

Soft Material Surface Wetting

When analyzing the soft material wetting, it is paramount to look at different aspects of the wetting since different physics explains the different wetting characteristics. In this section, we will look at the hemiwicking velocity throughout the array and initially from the reservoir to the array, diffusion throughout the array, the inertial wetting results, and deformations of the soft material pillars.

Hemiwicking Velocity

The results of the hemiwicking experiments are shown in Fig. 3.6 (a) - (c). A trend that should be noted is the decrease in the hemiwicking velocity as the stiffness of the samples decrease. With all of the working fluids having a similar surface tension, the spacing between the more stiff and less stiff surfaces appear to be the same for the different experiments conducted. The phenomenons of viscoelastic braking [119, 120, 116] and the "stick-slip" motion [117, 118, 102] that have recently been observed in previous investigations can also provide an explanation for the observed drop in wicking velocity. Another important aspect that needs to be investigated is a comparison of the PDMS wicking samples to the wicking data of stiffer samples. The comparison with Si, Norland Optical Adhesive 61 (NOA) (E $\sim$ 200 MPa), and JB-Weld (E $\sim$ 6 GPa) are provided in Fig. 3.6 (a) - (c) [87]. The data gathered for Si was only found for ethanol, which is why the comparison data for Si is only provided for ethanol. Regardless, when comparing the PDMS data to the stiffer hemiwicking samples, it is seen that the change is hemiwicking velocity is not just relative to PDMS. This shows that overall the gap between the model and the observed velocity, even for the stiffest of samples, is brought upon by the change in stiffness. This reveals significant impact not just as the PDMS gets less stiff, but even using a soft material with a stiffness of 2 MPa can

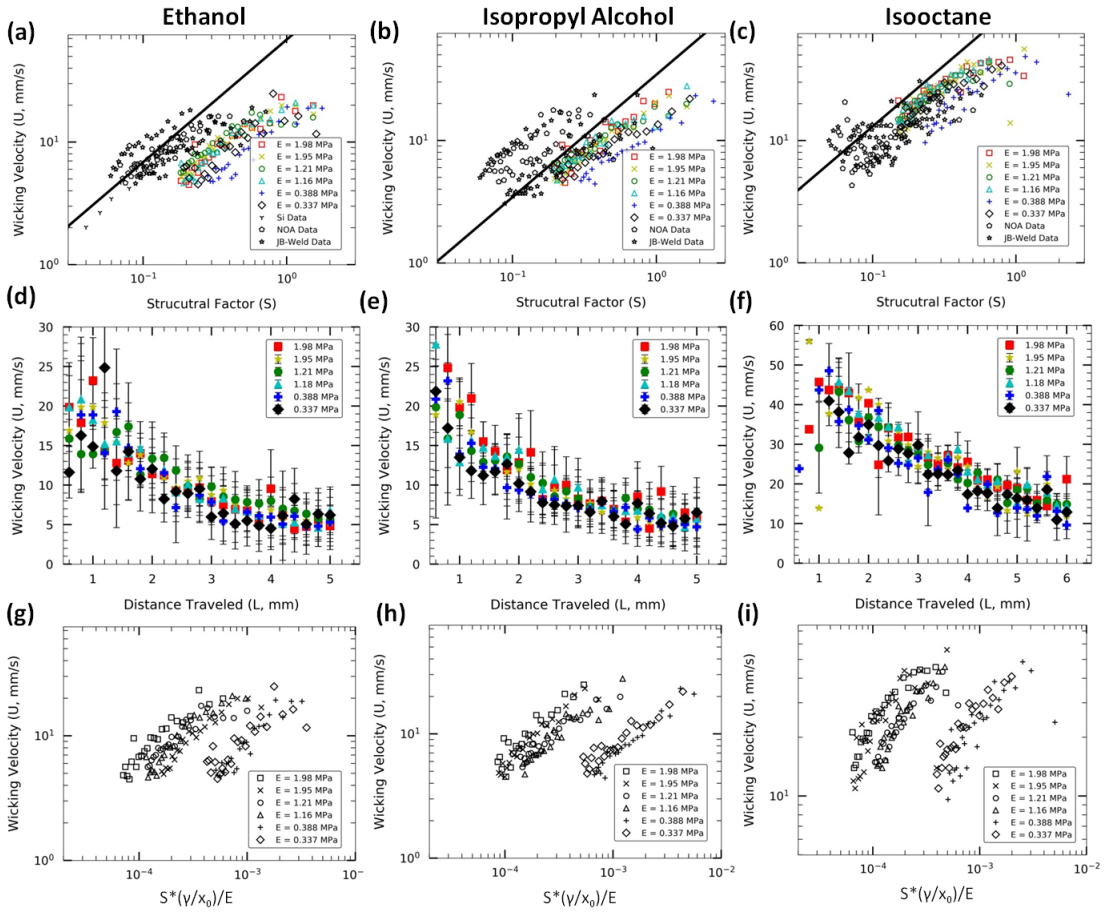

Figure 3.6: (a) - (c) The hemwicking velocity versus the liquid-surface factor for ethanol, isopropyl alcohol, and isooctane, respectively. the model lines presented in the graphs is based on Equation 3.5 from the previous chapter. (d) - (f) The velocity of ethanol, isopropyl alcohol, and isooctane, respectively, as function of the distance traveled by the working fluids in the hemiwicking array (g) - (i) The wicking velocity versus a modified liquid-surface factor introduced through Equation 3.21 for ethanol, isopropyl alcohol, and isooctane, respectively

impact the wicking performance. This fact amplifies the findings further discussed in this chapter where the changes in performance is not just reflected in a relative change of performance within the PDMS samples, but an overall change in performance when compared to more stiff samples.

This trend is further explored when the velocity of the working fluid is plotted against the distance

the working fluid has traveled in the array, which is displayed in Fig. 3.6 (d) - (f). A few trends are reinforced when analyzing the wicking performance through this parameter; namely the same dynamics that dictate the wicking velocity for all samples despite the change in stiffness and the overall decrease in wicking velocity for the less stiff samples. In general throughout the first five mm of the wicking array, the more stiff samples exhibited the highest wicking velocity. Beyond five mm, especially for the less stiff samples, zippering begins to occur. Zippering is the phenomenon is wetting where the velocity normal to the direction of wetting no longer is negligible and must be accounted for in analysis [127]. However, it is noticed that all the trials for isooctane go to six millimeters. This is due to the enhanced wetting performance of isooctane as compared to ethanol and isopropyl alcohol, leading the zippering to occur deeper into the wicking array. This trend can begin in to seen at the end of the investigated distance into the array. However, from looking at the velocity against both the distance traveled and the structual factor, it can be determined that the stiffness of the soft materials does play a role in the overall hemiwicking performance.

In an attempt to scale the velocity with the stiffness of the sample, a normalizing term is introduced to the solid-liquid structure factor. This normalizing term is the ratio of the interfacial forces (i.e. surface tension and meniscus extension) to the stiffness of the sample (i.e. Young's Modulus). This normalizing term is presented in the following equation.

$$U \sim S\frac{E}{\frac{\gamma}{x_0}} \tag{3.21}$$

Figure 3.6 (g) - (i) reveals the velocity results with the normalized term incorporated to the structure factor. When the factor is included, two groups begin to form between the samples with a Youngs Modulus above 1 MPa and the samples with a Youngs Modulus below this value. This reinforces what is presented with the original velocity data where the stiffness of the soft materials does play a role in the wicking performance.

Hemiwicking Diffusion

The effect of the stiffness of soft materials on hemiwicking performance is further enforced in the diffusion of the fluid through the pillar array. Figure 3.7 (a) - (c) displayed the distance traveled by the fluid through the array as a function of the square root of time. It was plotted as such due to the well established diffusion relationship.

$$L \sim (Dt)^{1/2} \tag{3.22}$$

where D is a diffusion coefficient. As expected from Equation 3.22, a linear relationship between those two variables is established, where the diffusion constant can be found by squaring the slope of the best fit linear line of zero intercept through the data. It can clearly be discerned that as the stiffness of the sample decreases, the diffusion constant for the fluid traveling through the array also decreases for all working fluids. When comparing the most stiff sample to the least stiff sample, there is a change of diffusion of 29.2 %, 28.0 %, and 23.6 % for ethanol, isopropyl alcohol, and isooctane, respectively. To demonstrate this concept further, the normalized diffusion lengths were plotted as a function of the Young's Modulus of the different samples, as shown in Fig. 3.7 (d). The normalized diffusion for this dissertation is defined as the the diffusion constant derived through the linear best fits from Fig. 3.7 (a) - (c) multiplied by the ratio of the fluid dynamic viscosity to the surface tension. This plot reveals a significant drop off in the normalized diffusion length once the sample has a Young's Modulus below 1 MPa.

Combining the diffusion results with the wetting velocity results reveals the impact that the stiffness can have on the overall hemiwicking velocity. This result reveals the importance of understanding how the wetting motion of a fluid will impact the overall surface and how any changes in the surface can impact the wetting performance. Even though it was not observed in the images or

videos taken for this dissertation, viscoelastic braking or possible surface deformations similar to what is seen with an evaporating sessile droplet may be impacting the overall wetting velocity and diffusion. New models that incorporate the stiffness of the materials will need to be developed in order to properly predict the wetting performance, since there is a new energy association with the possible deformation of a surface.

Relating these results to the upcoming technology of flexible heat pipes reveals the importance of understanding and predicting the wetting behavior. This observed wicking performance degragation due to the softness of the materials can lead to an overall impact on the heat transfer performance. The possible viscoelastic braking or surface deformation can impede a liquids ability to wet a nucleation site at higher heat fluxes, leading to an overall lower critical heat flux on microstructured surfaces. The findings presented in Fig. 3.6 and 3.7 reveal the importance of taking into account the stiffness for future cooling technologies.

Initial Hemiwicking Velocity

Along with the hemiwicking velocity and diffusion, the initial velocity is analyzed to investigate whether the stiffness has an effect on the initial wetting velocity. The results of the initial wetting velocity is revealed in Fig. 3.8. When analyzing both the maximum velocity and the average velocity of the working fluid across the first row in the microstructure array, a similar trend is seen, though the performance of isooctane for the maximum velocity is much greater compared to the average velocity relative to isopropyl alcohol and ethanol. This is mostly due to the greater variation of the velocity of fluid across the first row in ethanol and isopropyl alcohol compared to isooctane. However, similar to the velocity throughout the array, there is an apparent relationship between the initial wetting velocity and the stiffness of the soft materials. This consistency is results reveals how the impact of the soft materials changes every aspect of the hemiwicking

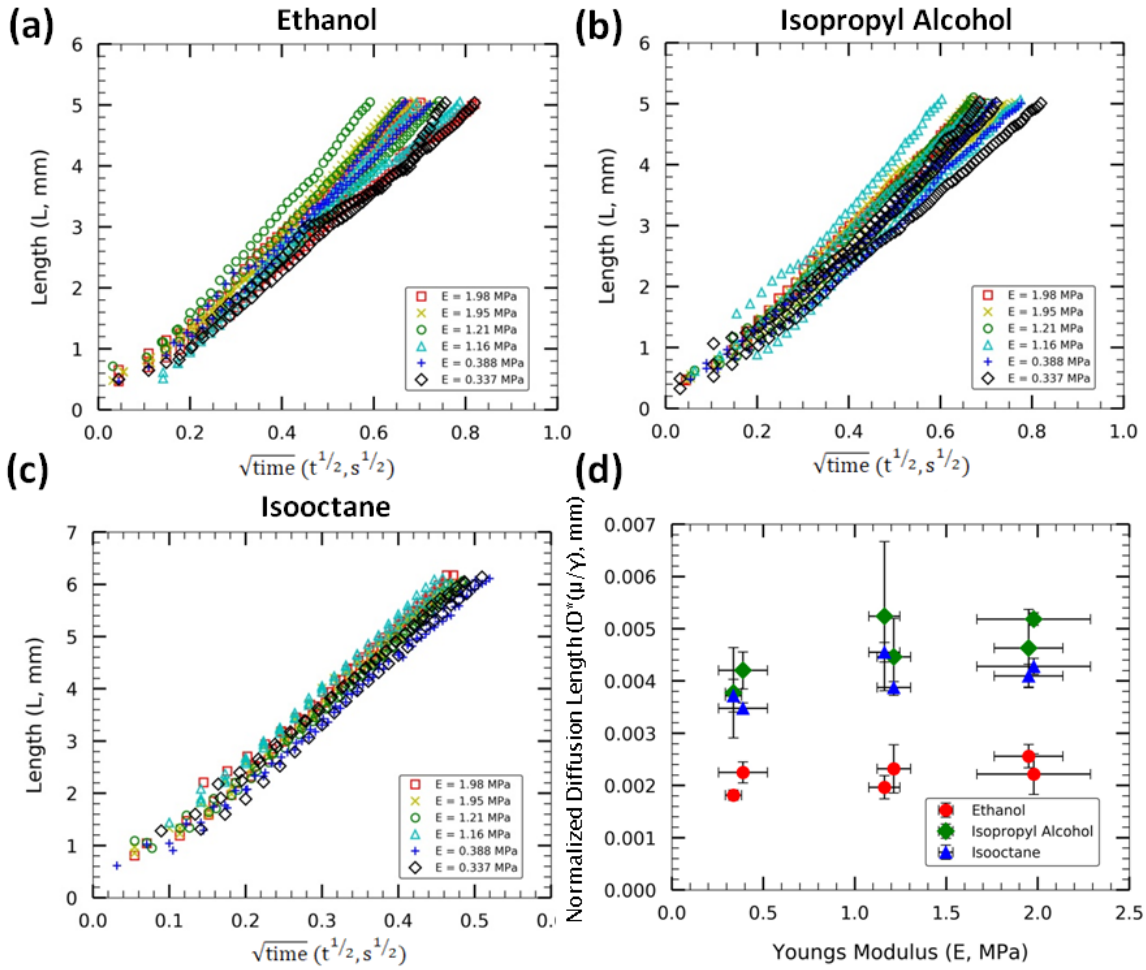

Figure 3.7: (a) - (c) The distance traveled by the working fluid versus the square root of time, where the initial time is where the working fluid begins to wick from the fluid reservoir. The results shown are for ethanol, isopropyl alcohol, and isooctane, respectively. (d) The normalized diffusion length versus the Youngs Modulus for the samples

performance.

Analyzing the initial velocity results provide even deeper insight into how soft material hemi-wicking structures can perform when rewetting a nucleation site. The initial velocity of a fluid has already shown to be a component in the maximum thermal transport a fluid can perform on

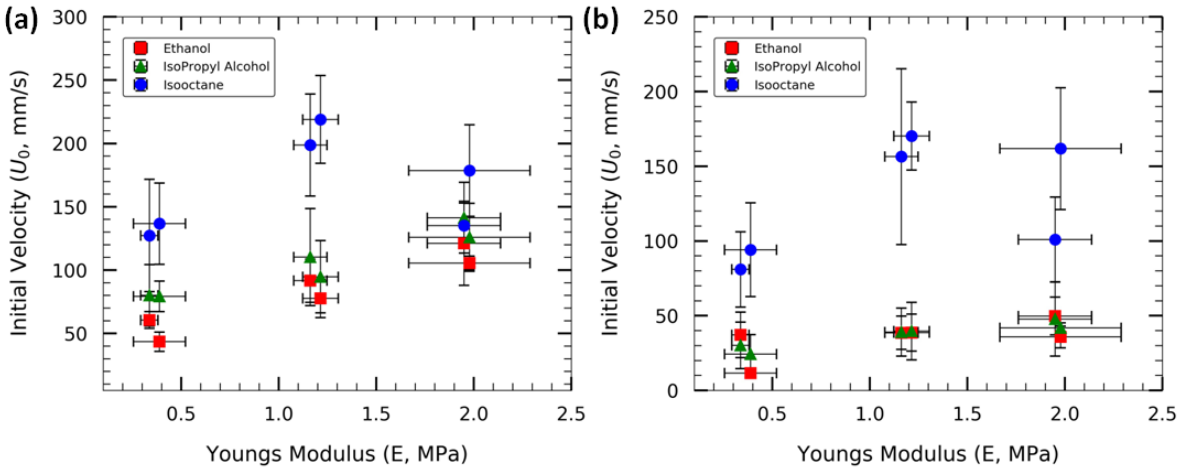

Figure 3.8: The initial hemiwicking velocity results for ethanol, isopropyl alcohol, and isooctane as a function versus the stiffness of the PDMS samples. The presented results are for (a) the maximum observed velocity and (b) the average observed velocity

a heated surface. This is due to the initial velocity being a portrayal of the desire of the fluid molecules to interact with the surface. The higher the initial velocity of a fluid is, the more the fluid particles energetically desire to interact with the surface molecules . In thermal applications, this correlates to the critical heat flux a surface can experience since more thermal energy will be required to overcome the natural wetting energy between the surface and the fluid. Therefore, the decrease in the initial wetting velocity as the stiffness decreases reveals that the less stiff samples may not be as effective in cooling a surface and will experience a lower critical heat flux compared to more stiff samples.

Soft Materials Inertial Wetting

For consistency, the inertial wetting results for the soft material surfaces were also gathered to compare with the hemiwicking results and with recent inertial wetting results of soft wetting done

by other research groups [92, 114, 115]. These results are displayed in Fig. 3.9. It can be determined that for all three fluids that the stiffness of the surface does not play a clear role in the inertial results, unlike the hemiwicking results. This aligns well with findings previously discovered from other research groups, where the main difference observed was the distanced traveled where the wetting transitions from inertial to viscous wetting.

Important observations can be made when comparing the inertial wetting results to the hemiwicking results presented previously in this chapter. First is the consistency compared to other studies where the stiffness did not play a significant impact on the inertial wetting performance. This consistency not only verifies the experimental methods used to measure the velocity, but reinforces the main impact of soft materials presented in the hemiwicking results. When comparing the inertial wetting data to the hemiwicking data, the different time scales for each wetting region needs to be taken into account (see Equations 3.19 and 3.18). Namely, the difference in the fluid properties that predict the fluid behavior. Since the differences are only seen with the hemiwicking results, the viscosity plays a significant impact in the degragation of the hemiwicking performance, since the viscosity is not included in the inertial wetting time scale (as compared to the surface tension, which is incorporated in both time scales). This further reinforces the hypothesis of visco-elastic braking hindering the wicking performance for soft materials.

Another interesting observation can be made when comparing the inertial wetting results to that of stiffer materials. It can be determined from Fig. 3.9 that, unlike the hemiwicking results, there is no difference between the inertial wetting performance for all the working fluids for the PDMS samples as compared to the stiffer samples. This raises some questions regarding the dynamics that occur within the inertial wetting regime, namely the amount of turbulence that occurs within the first few milliseconds of a droplet interacting with the surface. Further research will need to be conducted to fully understand the fluid dynamics that occur within the first milliseconds of a droplet interacting with the surface.

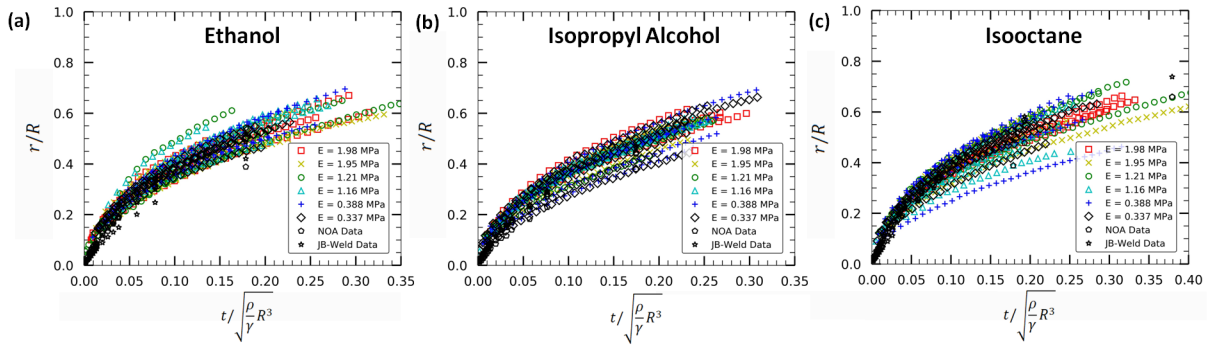

Figure 3.9: The normalized distance traveled by the fluid with respect to the initial droplet size versus the normalized time from contact with the surface with respect to the inertial time wetting scale (see Eqn 3.18). The presented results are for (a) ethanol, (b) isopropyl alcohol, and (c) isooctane. For all three trails, comparisons to Norland Optical Adhesive (NOA) and JB-Weld are provided with the same working fluids

Pillar Deformation

One interesting discovery that was made in the process of soft material hemiwicking was the observation of the bending of the pillars during the fluid evaporation. For these experiments, a PDMS EcoFlex hybrid sample was created in order to create a sample of even lower stiffness (E = 0.228 MPa). Pictures of the bending process are provided in Fig. 3.10. From the images taken, it can be seen that the deformations only occur while the working fluid are evaporating from the wicking array and do not occur while the fluid moves across the array. This shows how much greater the interfacial forces impact the stability of the pillars compared to the kinetic and viscous forces brought upon by the wicking of the fluid. When analyzing a design of a heat pipe with wicking structures, this finding is of great interest for the heated region of the heat pipe, where the working fluid will evaporate more often.

In order to fully characterize these deformations, an energy balance was performed between the proposed torques acting on a pillar and the inherent desire for a pillar to remain upright. From the

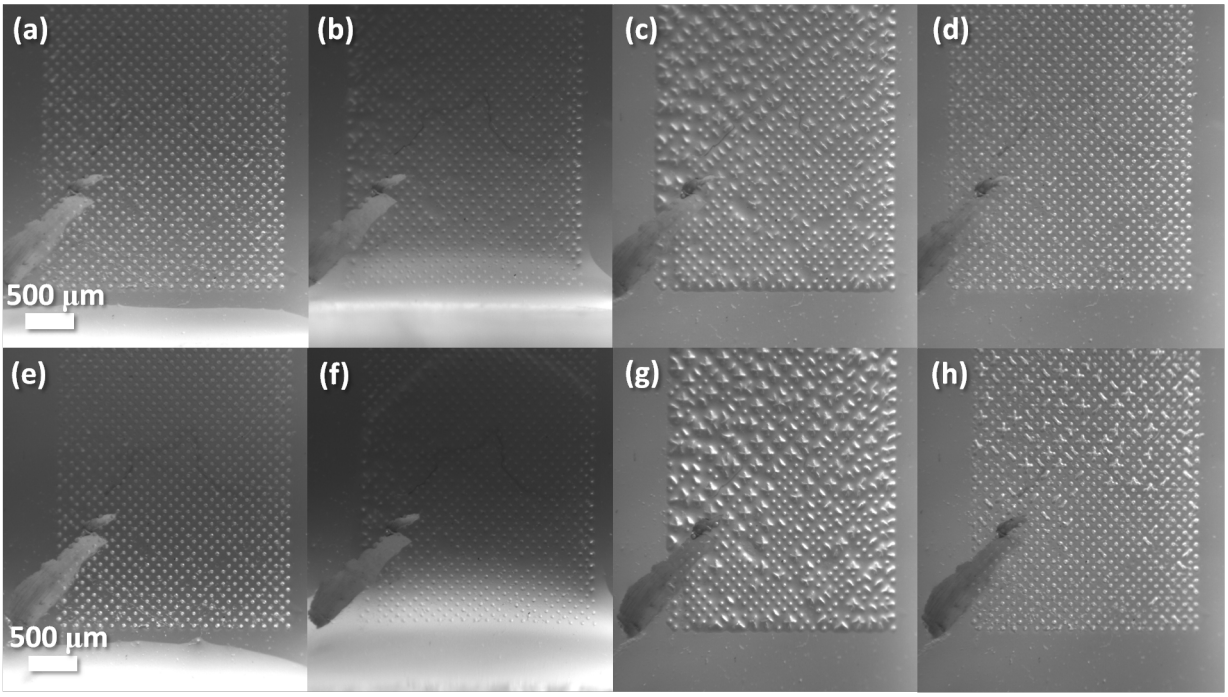

Figure 3.10: Frames of the different stages of wicking and pillar bending observed on a PDMS/EcoFlex combined sample. (a) -(d) is the observed behavior for ethanol while (e) - (h) is the observed behavior for isopropyl alcohol. The stages of the wicking process shown in both figures from left to right is before wicking, fluid wicking, pillar bending, and pillar restoration.

energy balance, the following models for the Youngs Modulus and the time scale were derived.

$$E \sim \frac{16\gamma h^3 \cos^2\theta}{\pi r^3 (s/2 - R)} \tag{3.23}$$

$$t_{mod} \sim (1 - \cos\theta)\frac{2\rho r h (s - 2r)\delta h_{fg}}{k_f \Delta T} \tag{3.24}$$

When looking at the scale provided in Equation 3.23, deformations for ethanol and isopropyl alcohol would both occur if the Youngs Moudlus of the sample was roughly around 550 kPa at

the most (i.e. if θ is 90 degrees). This is close to what is observed with our experiments, though the none of the PDMS samples exhibit deformation with ethanol. However, this scale provides an important characteristic for soft hemiwicking design to when deformations of the structures would be expected.

It should also be noted that in multiple scenarios throughout the array that four pillars will deform toward a center point between the four pillars. This provides evidence that the bending from one pillar can influence the bending direction of the adjacent pillars, since it is already known that disjointing energies and pressures are affected by the curvature of a thin film. The structures will go from upright to deformed in 2 to 3 milliseconds. As the fluid begins to fully evaporate from the surface, the pillars begin to return to their original shape within a millisecond. This shows that the noticed deformation will not lead to permanent deformation. The same effect was observed throughout multiple trials, showing that the deformation will continue to occur regardless of the previous deformation of the other trials.

PVA Monolayer Wetting Changes on PDMS

Table 3.3: The Observed Change in the Meniscus Extension from the Pillars with Ethanol Between State 1 and State 2

Sample	x_0 (μm, State 1)	x_0 (μm, State 2)
A	18.8	No Wick
B	37.2	40.2
C	34.9	36.4
D	29.4	34.0
E	27.8	31.4
F	31.9	38.6

The first results that will be discussed will be when a monolayer of PVA was applied on different thin-film metals. Two main areas will be analyzed when looking at the effect of the monolayer on

Table 3.4: The Observed Change in the Meniscus Extension from the Pillars with Isooctane Between State 1 and State 2

Sample	x_0 (μm, State 1)	x_0 (μm, State 2)
F	42.4	46.1
G	40.5	35.9
H	43.5	43.4
I	37.3	37.8

wetting performance; the meniscus extension and the wicking velocity. The meniscus extension for ethanol and isooctane at the different states are presented in Table 3.3 and 3.4, respectively. For all of the samples where ethanol wicked and some of the samples with isooctane that the meniscus distance increase as the effect of the PVA monolayer on the samples decreased. This reveals a change in the inter molecular mechanics within the meniscus as a result of the change in the surface chemistry. This is especially significant when taking into account the curvature of an evaporating thin-film. It has been found that the total heat transfer possible in this region is dependent on the curvature of the evaporating thin-film [128]. Seeing a change in the meniscus extension off of the last array shows a change in the curvature of the evaporating region off of the hemiwicking array, showing a change in the thermal transport potential based on the surface chemistry.

These results are significant in understanding in the impact the surface chemistry has on the wetting performance. As discussed earlier in this chapter, Krishnan et al. has conducted a study finding how the interfacial forces impact the wetting performance [87]. That study predicted that the meniscus extension is inversely proportional to the wicking performance. Relating the findings of that study to the change in the meniscus extension change displayed in Tables 3.3 and 3.4, it can be said that as the effect of the PVA wore off, the hemiwicking velocity will decrease for both ethanol and isooctane.

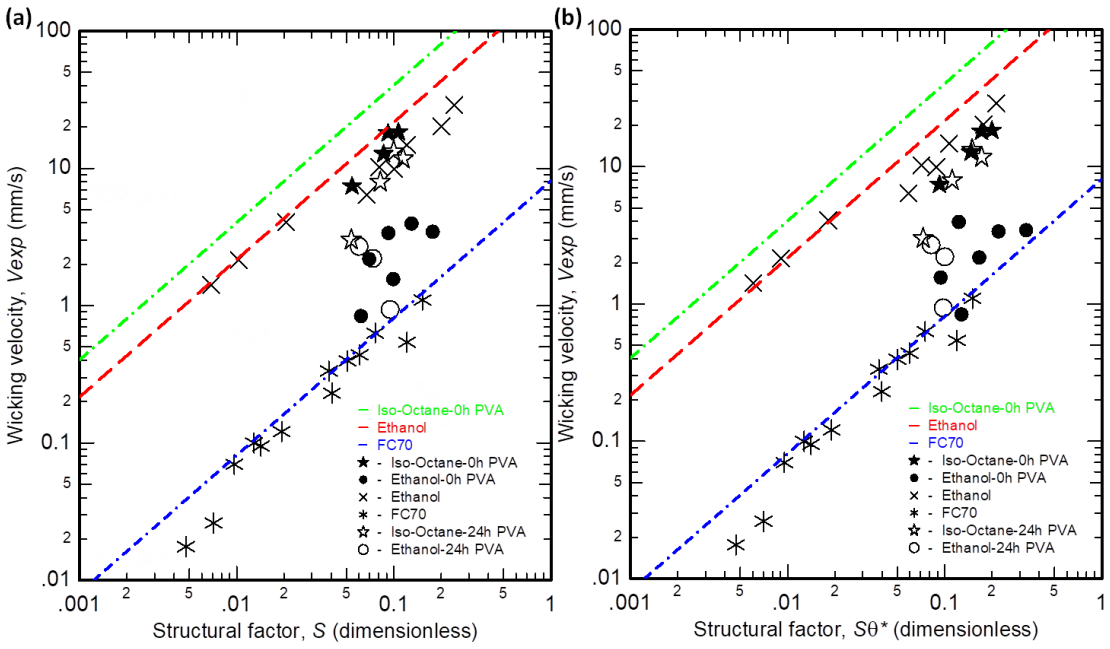

Figure 3.11: (a) The hemiwicking velocity results for the thin-film metal samples after PVA applicatoin and 24 hours after application. Data gathered from FS samples are also provided in this Figure for comparison. (b) The hemiwicking results when introducing a correcting term taking into account the wetting characteristics at the different states.

The velocity results for the two different states are displayed in Fig. 3.11. A couple major observations can be detected from the PVA wicking velocity results. First is the significant decrease in the velocity between State 1 and State 2. In fact, it can be noticed that there are more data points for right after PVA application than there is for 24 hours after application. This is due to the working fluids stopping motion at an earlier length 24 hours after application. This is due to the decrease in capillary action since the fluid is not as energetically attractive to the surface as before.

In an attempt to take into account the surface wetting, a surface term, θ^* is introduced. This term

is defined through the following equation:

$$\theta^* = \frac{\theta_{adv} - \theta_{rec}}{\theta_{eq}} \tag{3.25}$$

The velocity versus the modified liquid-surface factor term is presented in Fig. 3.11 (b). It is observed that, even though it is not a perfect relationship, that introducing the modified term better predicted the observed velocity on the samples. This finding reveals the importance of understanding the intermolecular interactions between the liquid and solid molecules at the surface. It was mentioned in the literature review that the initial wetting velocity of a fluid plays a significant role in the heat transfer performance of a fluid. This observed change in the wetting velocity therefore reveals that a change in the intermolecular interactions through surface coatings can impact the overall thermal transport performance of modern cooling devices.

CHAPTER 4: CONTROLLABLE SURFACE WETTING

Literature Review

Based on the results presented in the previous chapter,the ability to control the surface wetting that occurs on the surface is ideal for different heat transfer systems. For this dissertation, a look at metamaterials and photoreactive surface coatings will be presented in the literature review.

Metamaterials

One area of controllable surface energy has arisen with the popularity of metamaterials. Metamaterials are a new branch of materials that exhibit behaviors not naturally seen because of atomic interactions at the nanoscale [129, 130]. For instance, some of the characteristics of metameterials that was of interest was the epsilon near zero (ENZ) points and negative index of refractions [131, 132]. As a result, metamaterials have gained a great amount of attention for their unique properties and their wide range of applications, including high resolution imaging, thermal effusers, photovoltaic cells, and biomedical devices [129, 130, 133, 134].

These unique characteristics are attributed to the engineering of the inter-atomic van der Walls forces between the different thin film metals. There are three main components that contribute to the overall van der Walls forces; the Keesom potential, the Debye potential, and the London potential [135]. The Keesom potential arises from the dipole-dipole interactions between the molecules, which can be calculated through the following equation [136].

$$w_k(r) = -\frac{(u_1 u_2)^2}{3(4\pi\varepsilon_0\varepsilon)^2 k_B T r^6} \tag{4.1}$$

where $w_k(r)$ is the Keesom potential, u_1 and u_2 are the dipole moments of the molecules, ε is the dielectric constant, k_B is the Boltzmann's Constant, T is the temperature, and r is the distance between molecules. The Debye potential is dipole-induced dipole interactions that are angle-averaged. The potential can be calculated through Equation 4.2 [135].

$$w_D(r) = -\frac{u_1^2\alpha_{02} + u_2^2\alpha_{01}}{(4\pi\varepsilon_0\varepsilon)^2 r^6} \tag{4.2}$$

where $w_D(r)$ is the Debye potential and α_{01} and α_{02} are the electronic polarizabilities of the involved molecules. Lastly, the London potential, also known as the dispersion force, is unique in the fact that it is present between all molecules and is considered the most important [135]. The potential can be calculated through the following equation [137].

$$w_L(r) = -\frac{3}{2}\frac{\alpha_{02}\alpha_{01}}{(4\pi\varepsilon_0)^2 r^6}\frac{h\nu_1\nu_2}{\nu_1+\nu_2} \tag{4.3}$$

where h is Planck's constant and ν_1 and ν_2 are the ionization frequencies. Therefore, the total interatomic potential can be found by combining Equations 4.1, 4.2, and 4.3. From this combination, two main contributions are noted; one between every molecule (London dispersion) and one that arises from polarities (Keesom and Debye).

Based off of the aforementioned potential, the van der Waals force can be found between two particles. However, these interatomic forces vary from one geometrical set up to the next [138]. For instance, the van der Waals force for two spheres can be calculated as [135].

$$F = -\frac{A_H}{6D^2}\frac{R_1R_2}{R_1+R_2} \tag{4.4}$$

where R_1 and R_2 are the sizes of the particles and A_H is known as the Hamaker constant. This constant was introduced by Hamaker who originally defined the constant through the following

equation [139].

$$A_H = \pi^2 C \rho_1 \rho_2 \tag{4.5}$$

where C is a coefficient based on particle interaction and ρ_1 and ρ_2 are the number densities of the particles in question.

Studies have been conducted to discover how the inter-atomic forces which give metamaterials its unique properties affect the surface wetting that occurs on the material. Popular methods conducted to find the affect is finding the contact angle changes with different thin-film layerings on a substrate [140]. Along with different layerings, implementation of different surface conditions were also conducted to see if the surface conditions can amplify the affects of the inter-atomic forces [141]. Based on the unique characteristics that have been found in different studies based on the interatomic forces, this dissertation aims to engineer to interatomic forces and relate that to changes in the surface wetting.

Photoreactive Surface Conditions

Another method that has gained popularity in controlling the surface chemistry is the use of photoreactive surface coatings on common surfaces. These surface coatings, such as spiropyran and photoacids, are able to achieve this change in the surface chemistry through a change in the chemical structures under different light conditions [142]. Different applications, including chemical sensing and molecular photoswitches, implement the use of these photoreactive coatings since light sources are easy to obtain and exhibit no harm to biological environments [143, 144]. To achieve this change, different methods of applications have been used to create the change in the contact angle. For instance, the effect of applying the photoreactive coatings on smooth and rough surfaces have been investigated [145, 146]. Along with different forms of applications, the effect

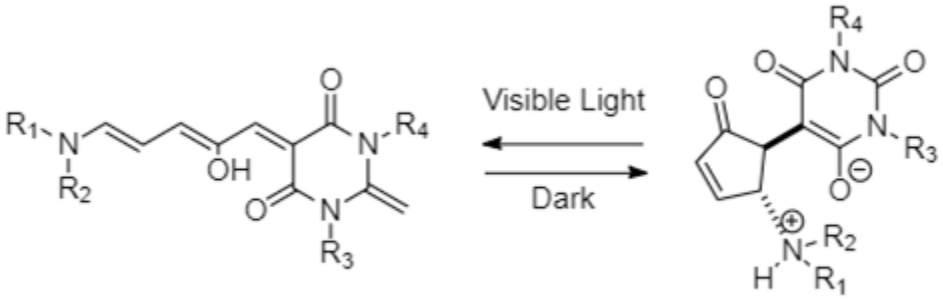

Figure 4.1: The change in molecular structure for a donor acceptor Stenhouse adduct (DASA) based on light

of concentration of the photoreactive compound attached to a surface has also been studied [147].

These methods work due to the reorientation of the molecular compounds that occur once the molecule is exposed to light. An example of a molecular change based on light is presented in Fig. 4.1 [148] with DASA. It can be observed that as the bonds in the molecule reorient themselves based on the light, additional charges become exposed. These additional charges interact with the polar water molecules on the surface, affecting the overall contact angle and wetting characteristics along with inherent electric properties.

Recent studies have been conducted over the past few decades with different photoreactive compounds in different areas. These different compounds include the aforementioned photoacid and DASA along with spiroyran [142, 148, 149]. Each type of different chemical can be used for different kinds of surfaces and various kinds of applications, such as nanoparticles and rods [150, 151]. These different kinds of applications have allowed this kind of technology to be used across a variety of surfaces, include polymers [152, 153, 154]. However, research has yet to be performed on microstructured surfaces. Based on the changes in wetting characteristics based on the contact an-

gle, utilizing these photosensitive coatings can be useful for changing the wetting characteristics, therefore changing the total thermal transport potential of a cooling fluid on a heated surface.

Research Methodology

To test the concept of controlling surface wetting, two separate scenarios were analyzed. First, thin-film hyperbolic metamaterials were fabricated to capture the change in surface energy and intermolecular forces as function of strain. The changes in the surface energy were characterized through measuring the advancing, receding, and equilibrium angle of various fluid of different polarities along with tracking the changes in the reflectance of the surface. Second, different samples were treated with spiropyran and the changes in the surface wetting were tracked through recording the changes on the contact angle.

Metamaterials Experimentation

Custom hyperbolic metamaterials were fabricated at the Air Force Research Lab in Dayton, Ohio through the use of an multi-gun magnetron sputtering system. The hyperbolic metamaterials were made through stacking thin-films of Tungsten (W), Titanium Nitride (TiN), and Hafnium Dioxide (HfO_2). These samples were deposited at various configurations and volume fractions to record any changes in the intermolecular forces and behavior of the metamaterials under strain. To accomplish the strain experiments desired for these robust metaterials, the thin-films stacks were deposited on pieces of Kapton Tape. Figure 4.2 shows a transmission electron spectroscopy (TEM) image of the thin film stacks after deposition. This was performed by attaching the Kapton piece onto a more sturdy substrate, such as silicon dioxide or sapphire. After the deposition process was completed, the Kapton tape was removed from the robust substrate, leaving a sample of metamaterial deposited

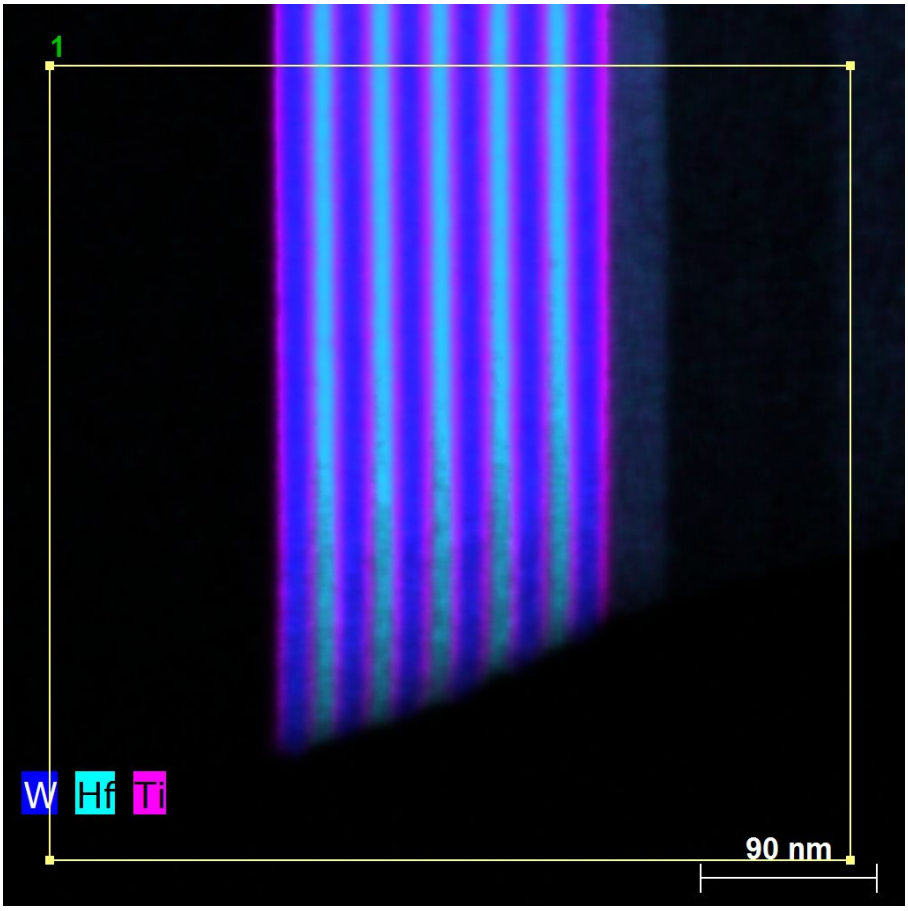

Figure 4.2: A transmission electron spectroscopy (TEM) image of one of the metamaterial samples after deposition. This metamaterial was created through stacking thin-films of Tungsten, Hafnium Dioxide, and Titanium Nitride on top of each other

on Kapton tape. This was desired since the Kapton tape could be strained to the desired values without breaking, as compared to the silicon dioxide and sapphire substrates.

After the metamaterials were fabricated, two main experimental methods were performed to characterize the change in surface energy as a function of strain; reflectometry and contact angle measurements. A simple uni-axial strain apparatus was fabricated to provide the strain for the samples tested in this dissertation. A schematic of the strain apparatus is displayed in Fig. 4.3 (a) Both

ends of each samples are clamped down and tightened through the use of fasteners. One of the clamped ends are fixed and the other is placed on a translation stage (Sensitivity = 0.001"). As the translation stage is moved, the sample is extended the distance that the translation stage is traveled, creating the strain on the sample. A Point Grey Flea Camera is utilized to capture when the straining begins and how the sample is interacting under the different strains. The desirable strains for this study are approximately 0, 2, 4, 6, and 8 %.

An in-house reflectometer used in previous works conducted by our lab was utilized to investigate changes in the reflectivity of the sample as a function of strain [128, 155, 156]. Figure 4.3 (b) provides an illustration to how the reflectometer used for these experiments work. The light used in this dissertation covers the UV-Vis-IR range (250 nm $\leq \lambda \leq$ 950 nm) and comes from three light sources; a broadband light source (λ = 190-2500 nm) based on deuterium (26 W) and tungsten halogen (20 W) lamps, a broadband white light LED (λ = 400-800 nm), and a narrowband near-IR LED (λ = 400-800 nm). The light from all three sources are brought together through the use of a bifurcated optical fiber (UV Enhanced 250-1200 nm). The light is directed and collimated from the optical fiber to a parabolic mirror, which guides the light to a polarized beam splitter (PBS). The beam splitter brings the light to an infinite objective used to focus the light on the sample. The reflected light then gets collimated through the infinite objective, passes through the PBS and a pinhole in an Ag mirror to a UVFS plan convex lens (f = 20 mm). The lens focuses the light into a fiber optic which carries the reflected light to a spectrometer. The spectrometer is used to measure the intensity of the reflected light off of the sample. For the reflectometry measurements, the sample in the strain apparatus is placed in the reflectometer. The samples were placed at strains of approximately 0, 2, 4, 6, and 8 %. Also, to ensure the accuracy of the reflectivity results, a 10x and 50x infinite objective were used to observed the change in reflectivity over a large area on the sample along with smaller locations (i.e. within flakes on the surface).

Along with the reflectivity, any changes in the Hamaker constant were also detected by detecting

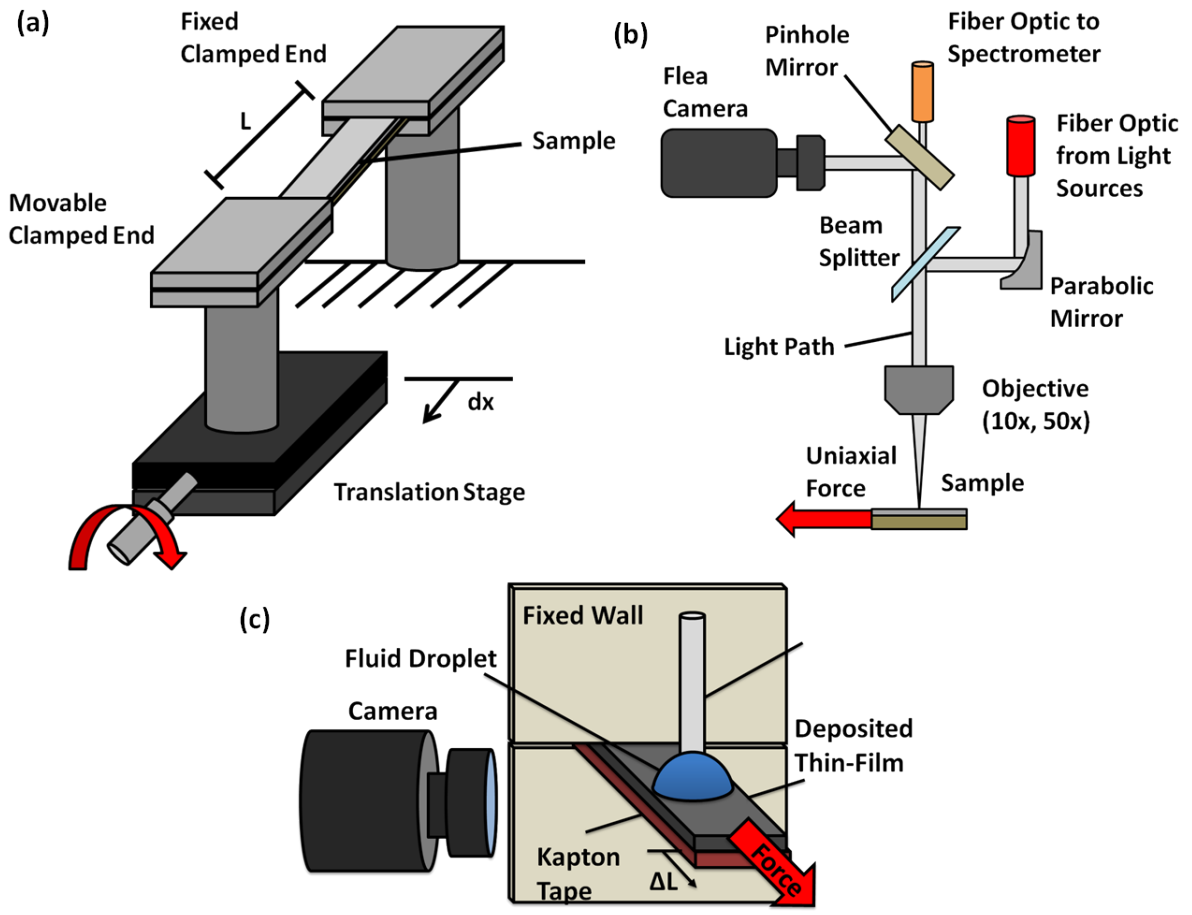

Figure 4.3: (a) A schematic of the simple strain apparatus used to provide uniaxial strain to the metamaterial experiments (b) The optics used to capture the change in the reflectance of the metamaterial samples as the sample is strained. (c) An illustration of the experiments conducted to capture the wetting characterization of the metamaterial samples under strain

the change in the wetting behaviors of water on the metamaterials surface as the surface encountered strain, as displayed in Fig. 4.3 (c). Similar to the reflectivity experiments, the wetting values were measured at 0, 2, 4, 6, and 8 %. The water was placed on and removed from the surface through the use of the syringe to ensure the wetting behavior would not have any effects from impact (i.e. We = 0). As the water is placed and sucked from the surface, a Flea Camera (Frame

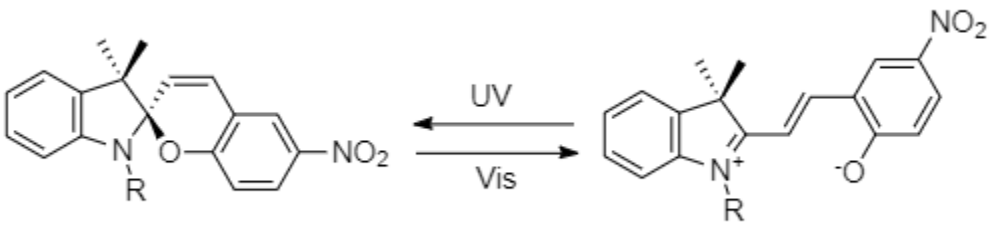

Figure 4.4: The change in molecular structure the spiropyran (SPCOOH) for this study

Rate = 2 fps) is used to capture the expansion and reduction of the water droplet on the surface.

A similar experimentation was conducted for fluids of different natural polarities to see the effect of the polarity of a fluid has on the change in contact angle as a function of strain. Theoretically, the changes in the wetting behavior of the fluid on the metamaterial surface will be different between a polar and non-polar fluid due to the polar components of the interatomic forces (i.e. the Keesom and Debye potentials). To investigate this, the advancing, receding, and equilibrium contact angle of water (γ^{LW} = 21.8 mJ/m^2, γ^{AB} = 51.0 mJ/m^2), formamide (γ^{LW} = 39.0 mJ/m^2, γ^{AB} = 19.0 mJ/m^2), and diiodomethane (γ^{LW} = 50.8 mJ/m^2, γ^{AB} = 0 mJ/m^2) was recorded as a strain was applied to different samples using the stain apparatus as previously described. With these fluid it's important to look at both the polar (γ^{AB}) and non polar (γ^{LW}) components of surface tension of the fluid.

Photoreactive Coatings

For the photoreactive coatings, an approach using an spiropyran attached to gold was utilized. The spiropyran of choice for this investigation was l-(β-carboxyethyl)-30,30-dimethyl-6-nitrospiro

(indoline-20,2[2H-1] benzopyran) (SPCOOH). The molecular structure change that allows for the change in contact angle is displayed in Fig. 4.4. A multiple step process was utilized to apply the spiropyran to the gold surface. First, a SAM of cystamine dihydrochloride was applied to the surface of the gold by submerged in a 5 mM aqueous solution of cystamine dihydrocholoride overnight. After the SAM is applied, the gold sample was placed in an ethanolic solution of 1-Ethyl-3-(3-dimethylaminopropyl)carbodiimide (EDC) and SPCOOH. The concentrations of EDC and SPCOOH are 0.01 M and $1x10^{-5}$ M, respectively, in ethanol. The sample was allowed to soak in the ethanol based solution overnight. Once the spiropyran was applied to the surface, the sample was exposed to UV light (λ = 365 nm) and visible light (λ = 535 nm) for activation of the hydroxide group which affects the surface chemistry. The sample was exposed to the different light sources for one minute each. After light exposure, the advancing, receding, and static contact angles were captured to characterize the wetting on the surface. The wetting angles were measured and recorded through the use of VSA Optima Video Contact Angle System.

Table 4.1: The Wicking Geometry for the Gold Microstructures Utilized for SPCOOH Experimentation

Sample	Shape	Pattern	S (μm)	H (μm)	d (μm)
JB-T	Half Cylinder	Square	50	12	20
JB-R	Half Cylinder	Hex	80	17.5	20

The microstructures investigated in this study were not fabricated in a similar manner as the microstructured surfaces mentioned in the previous section. These samples were fabricated through the use of lithography and thin-film deposition. For this study, different wicking geometries were utilized to further understand the amplification of the impact of wetting with SPCOOH based on geometry, similar to how pillar geometry dictates the hemiwicking behavior. The geometries of the samples are provided in Table 4.1. To capture the wetting characteristics, 6 μL droplets were placed on the surface and the contact angle was recorded. For each sample, the contact angle on

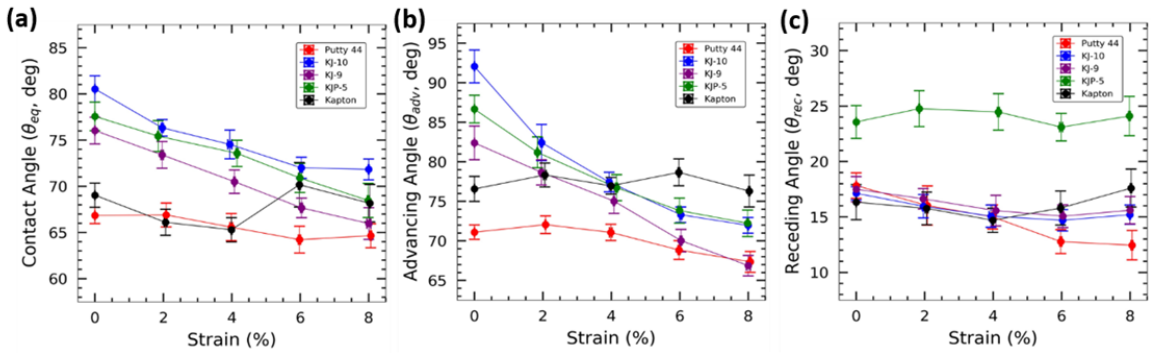

Figure 4.5: The wetting characterizations of the different thin film samples on Kapton tape as a function of strain. The wetting characteristics captured are the (a) static contact, (b) advancing, and (c) receding angles of water

bare gold and within the microstructures were recorded to characterize any difference in the change in wetting between the two surface conditions.

Findings

Changes in Wetting with Metamaterials

The results of the changes in wetting characteristics based on applying strain to a thin-film metamaterial are also going to be analyzed. The results for changes in the contact angle on the surface is presented in Fig. 4.5. It can be seen that for all of the metamaterials tested that as the strain increases, the advancing and equilibrium contact angles decrease. Even though these two wetting angles decrease, the receding angle remains constant throughout the experimentation. These changes are occurring due to the changes in the intermolecular interactions (i.e. Hamaker's constant). This is reinforced by the lack of change in wetting characteristics of the Kapton tape substrate.

It can also be observed that the change in the wetting characteristics vary between the different

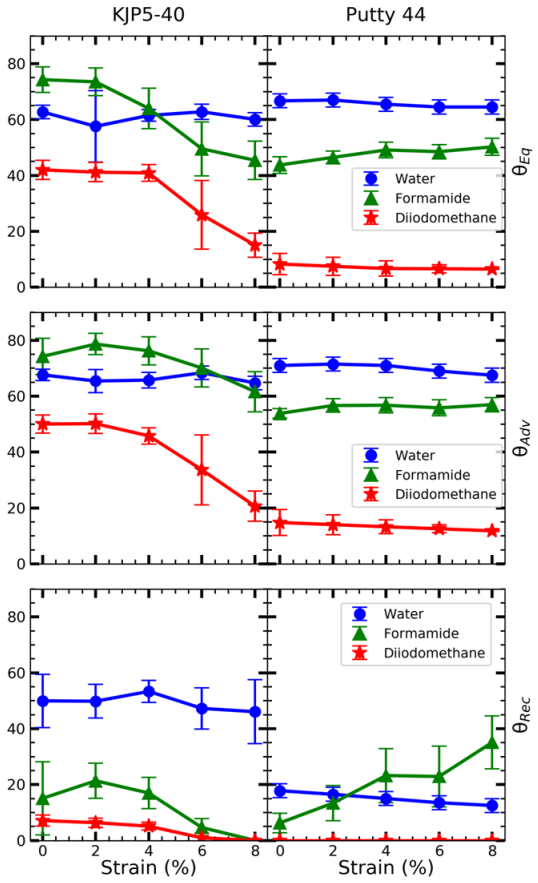

Figure 4.6: The advancing, receding, and equilibrium contact angles of water, formamide, and dioodomethane as a function of strain for KJP5-40 and Putty 44

samples. This is in part due to the differences in volume fractions and stackings between the samples, revealing that the intermolecular interactions throughout the thin-film stacks, not just on the surface, affect the overall wetting performance. When applying this for future cooling devices, this shows more of the importance of thin film stacking and how to take advantage of the different kinds of stacking.

The presence of the change in the intermolecular interactions is further enforced with testing the contact angle with fluids of various polarities. These wetting values are presented in Fig. 4.6

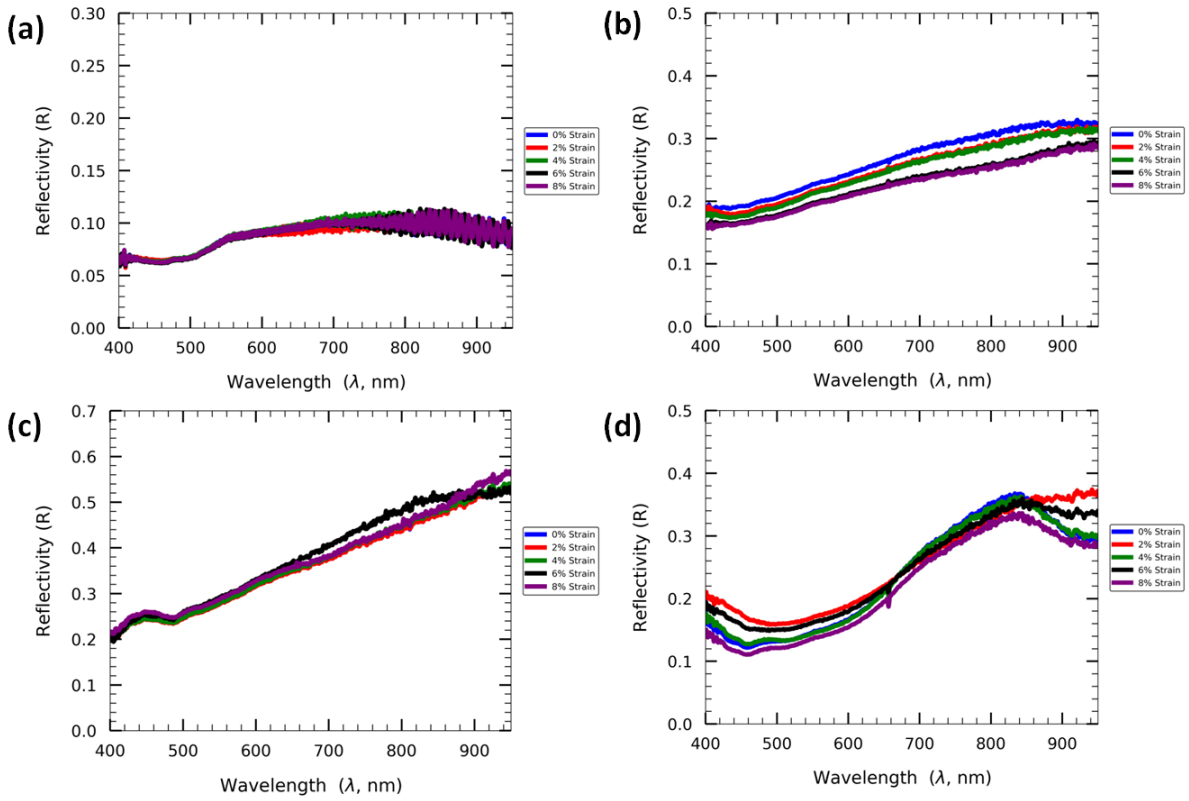

Figure 4.7: The change in reflectivity for (a) Kapton tape (b) Putty 44 (c) TiN and (d) TiN and HfO_2 stack layering at varying strains

for water, formamide, and dioodomethane. The changes in the wetting show a dipole-induced dipole coupling behavior between the thin-film metal stacks. This is namely shown through the difference in the advancing and receding angles. Another interseting occurence is the tendency toward super wetting for diiodomethane and great decrease in wetting angles for formamide on KJP5-40, but water not exhibiting the same behavior. This is brought upon by the polar behavior of water resisting the super wetting tendencies. With these difference, it can still be said that there is a change in the long term wetting behaviors for these two materials as strain is applied. This reinforces that findings in Fig. 4.5.

To further verify the impact of strain in changing the intermolecular interactions, the change in reflectance is also recorded and presented in Fig. 4.7. Similar to the wetting results, the reflectivity of the metamaterials change as the strain applied to the sample changes. Once again, this is known to be of the metamaterials due to the lack of change in reflectance for the Kapton tape substrate. This finding reinforces the wetting results since the changes in the reflectance are coming from a change in the intermolecular interactions in the thin film material, leading to a change in the way the light interacts with the surface.

Based on these metamatierals results, it can be concluded that implementing metamaterials can assist in increasing the overall heat transfer performance of a fluid through strain. Similar to the results presented earlier in this chapter with the PVA SAM and the SPCOOH coated surfaces, a change in the wetting performance translates to a change in the overall thermal performance. However, through the metamaterials results and the SPCOOH results, different ways to control the wetting is presented. This ability to control the surface wettting derives from an understanding of the molecular interactions both on the surface and throughout the metamaterial and taking advantage of the increased wetting performance.

Along with the effect of cooling that is occurring, the changes in the intermolecular interactions can also play a major role in the curvature of the evaporating thin-film meniscus. This region has gathered interest over the past few decades due to the enhanced cooling rate that is experienced in this area [128]. Due to the importance in this region, research has been conducted to characterize the curvature of the evaporating thin film region. Some of these predictions incorporate the intermolecular forces.

Table 4.2: The Changes in Contact Angle of Pure Gold Coated with SPCOOH Based on Light Exposure

Condition	Contact Angle (degrees)
After SPCOOH Application	63.8 ± 3.84
1 min UV light	64.2 ± 4.45
10 min Vis light	67.5 ± 2.17
1 min UV light	64.8 ± 3.08

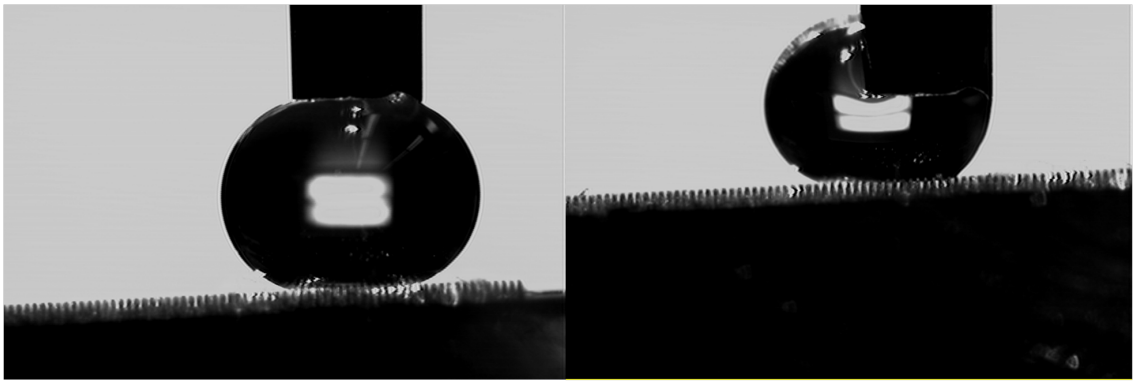

Figure 4.8: Two frames of water interacting with the hold microstructures before any chemical surface treatments were applied to the surface. The picture on the right depicts the "roll off" effect, which is an indication of the Cassie Baxter State of wetting for the microstructures

Photoreactive Coverings with Micro Structures

To properly understand the impact that the changes in the molecular structure of SPCOOH has on microstructured surfaces, it is desired to capture the wetting performance on bare gold. These results are provided in Table 4.2. It should be noted that for every step of the process, the contact angle was recorded to track how each step of surface modification impacted the wetting performance. It can be seen that on the pure gold samples that there is an overall change in the contact angle detected.

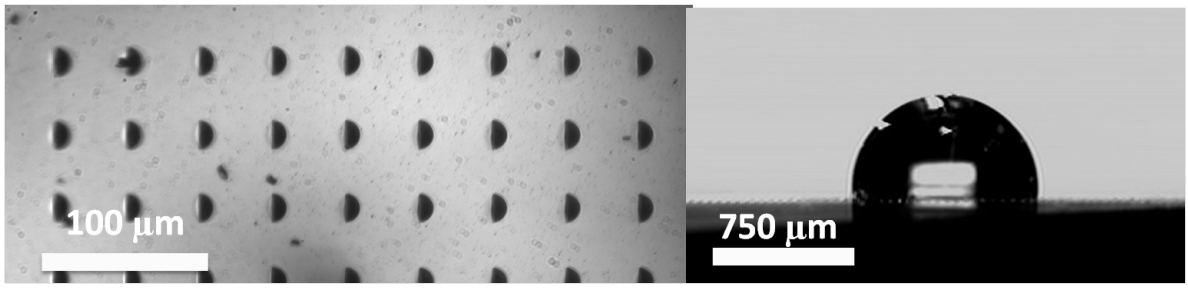

Figure 4.9: An overhead and side view of one of the samples of smaller wicking structures on the gold surface. It can be seen that the water droplets interact with these structures as compared to the previous structures

When the gold surface has microstructures, the wetting characteristics and the interactions the water has with the microstructures are recorded. An interesting finding is observed in Fig. 4.8. Even though there is a change in the surface chemistry, if the samples are too high or too close together, it will be energetically unfavorable for the water droplet to be on the pillars, showing an extreme Cassie-Baxter state. This shows a significance in looking at wetting, that the geometries of the pillars will play a significant impact in how the droplet behavior will change within a pillar array.

To further investigate the impacts that changes in the surface chemistry has on the microstructures, the wetting was recorded for smaller microstructured surfaces of varying geometries. A look at the samples utilized for this study are shown in Fig. 4.9. As compared to the tall wicking structures, the water was allowed to interact with the wicking structures, making it possible to detect the changes in wetting behavior. The values for the changes in wetting are displayed in Table 4.3 and 4.4. It can be seen that for the bare gold that the spiropyran is inducing a change in the contact angle. This shows that changes are being observed on a general gold sample as is expected.

However, interesting findings are in place for microstructured surfaces. It can be seen that the same

Table 4.3: The Changes in Contact Angles for Sample JB-T

	Trial 1		Trial 2	
Location on Sample	1 min UV	10 min Vis	1 min UV	10 min Vis
Bare Gold	68.41 $\pm$ 1.65	73.88 $\pm$ 2.57	72.7 $\pm$ 2.77	76.2 $\pm$ 4.14
Microstructures	70.64 $\pm$ 2.03	73.00 $\pm$ 1.37	71.8 $\pm$ 2.97	68.1 $\pm$ 2.07

Table 4.4: The Changes in Contact Angles for Sample JB-R

	Trial 1		Trial 2	
Location on Sample	1 min UV	10 min Vis	1 min UV	10 min Vis
Bare Gold	71.68 $\pm$ 2.50	72.8 $\pm$ 2.21	68.4 $\pm$ 6.25	71.1 $\pm$ 2.60
Microstructures	64.7 $\pm$ 4.25	69.1 $\pm$ 2.36	78.3 $\pm$ 2.47	77.5 $\pm$ 1.36

changes in wetting are observed within the microstructures. Hemiwicking was not observed with these samples, so the water droplet behavior within the wicking array through the contact angle is used to measure the change in wettability. It should be noted that there is a balance between the surface chemistry and the surface geometry that needs to be taken into account when designing these surface modifications for microstructures. For some structures where a water droplet will refuse to wet the surface, the molecular reorientation of SPCOOH was not enough for the droplet to wet the microstructures. This reveals that, even though there are chemical changes that make a surface more hydrophilic, these molecular changes still may not be enough to create an energetically favorable surface for the fluid to wet the microstructures.

CHAPTER 5: CONCLUSION

The findings presented in this dissertation bring to light the importance of surface conditions as technology demands thermal systems with higher cooling rates. The jet impingement results revealed a method in which the heating phenomenons could be measured within the thermal boundary layer through TDTR. Along with a unique way to measure the thermal transport in a popular cooling technique, two separate studies were conducted to analyze the impact of different surface conditions on the solid-fluid interaction. One approach was through utilizing soft materials on hemiwicking surfaces, demonstrating the importance of looking at possible surface deformations in impeding the hemiwicking performance. The other approach was through adjusting the surface chemistry of a hemiwicking surface to control the hemiwicking performance on a microstructures surface.

Combining all of these findings together yields a unique method and path in future research in further understanding the impact on interfacial interactions on the maximum heat flux a surface can experience. As the demand for greater thermal transport is required for future technologies, an understanding of the surface-fluid interactions on a heated surface within the thermal boundary layer will become more important to understand in order to maximize the thermal transport. Implementing methods, such as TDTR, will be useful in capturing such behaviors, not just in jet impingement, but in other modern cooling systems, such as spray cooling and passive heat pipes. The importance in capturing this behavior becomes greater as investigations on various surface treatments continue. For instance, if a metamaterial is placed on the surface and begins to experience strain, the inter molecular behavior will change, as demonstrated in this dissertation. These changes in behavior may lead to overall change in the thermal performance on the surface and the reasons for these changes will need to be detected capturing the fluidic behavior close to the surface.

Based on the work presented in this dissertation, a groundwork is laid for investigating thermal behaviors under the different surface conditions. Whether through various chemical surface coatings, newly fabricated metamateirals, or any other method of controlling the surface energy, the thermal performance can be recorded for these samples under various different conditions. Through the use of TDTR, the liquid-surface interactions can be observed, providing a unique method of detecting the changes in thermal performance close to the surface based on the changes in molecular interactions. Combining all of these methods together can help tackle some of the cooling challenges faced in industry today, paving the way for more powerful technology to emerge.

APPENDIX A: JET IMPINGEMENT ADDITIONAL INFORMATION

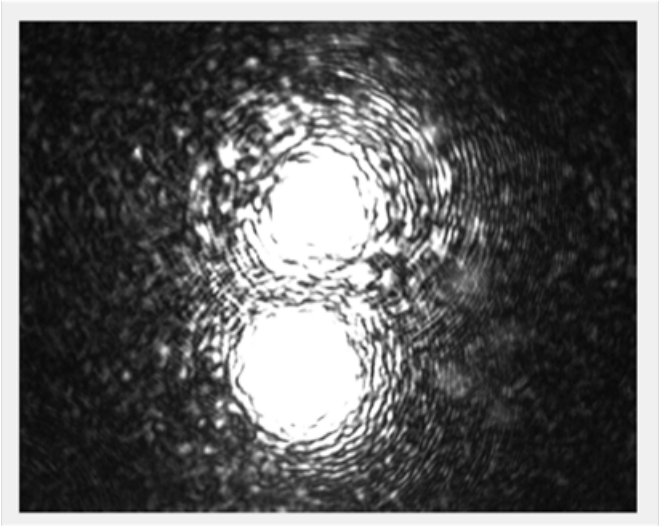

Figure A.1: A picture of both the pump and probe beams in the microchannel.

APPENDIX B: SOFT WETTING ADDITIONAL INFORMATION

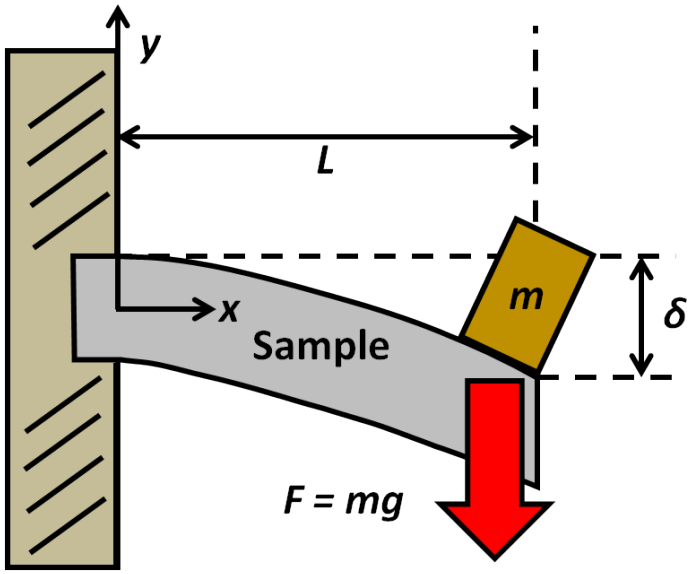

Figure B.1: A schematic of the cantilevered beam experimentation used to determine the Youngs Modulus of the PDMS Samples

Table B.1: The fabrication methods for the PDMS Samples for the study along with the corresponding Youngs Modulus

Sample	Mixing Ratio	Curing Time (Hours)	E (MPa)
1	10:1	1	1.21 ± 0.0910
2	10:1	3	1.16 ± 0.0854
3	15:1	1	0.388 ± 0.134
4	10:1	5	1.95 ± 0.188
5	20:1	1	0.337 ± 0.0443
6	9:1	5	1.98 ± 0.311

Table B.2: The meniscus extension values with the different working fluids on the samples used in this study

Sample	Working Fluid	Meniscus Extension ($x_0, \mu m$)	E_0 (γ/x_0, N/m^2)	E/E_0
1	Ethanol	26.44 ± 4.27	830.938	1456.186
1	Isopropyl Alcohol	26.28 ± 2.40	796.423	1519.293
1	Isooctane	20.94 ± 1.10	888.252	1362.226
2	Ethanol	27.18 ± 3.08	808.315	1435.084
2	Isopropyl Alcohol	25.61 ± 3.32	817.259	1419.379
2	Isooctane	27.85 ± 1.79	667.864	1736.881
3	Ethanol	27.53 ± 4.66	798.039	486.192
3	Isopropyl Alcohol	26.60 ± 2.77	786.842	493.614
3	Isooctane	24.71 ± 1.72	752.732	515.456
4	Ethanol	20.49 ± 2.31	1072.230	1818.640
4	Isopropyl Alcohol	20.61 ± 2.08	1015.526	1920.187
4	Isooctane	27.63 ± 2.27	673.181	2896.695
5	Ethanol	27.08 ± 2.02	811.300	415.383
5	Isopropyl Alcohol	26.65 ± 2.02	785.366	429.099
5	Isooctane	25.05 ± 1.81	742.515	453.863
6	Ethanol	26.73 ± 3.69	821.923	2408.985
6	Isopropyl Alcohol	25.13 ± 1.38	832.869	2377.325
6	Isooctane	30.18 ± 3.87	616.302	3212.711

APPENDIX C: DERIVATION OF SCALES USED FOR SOFT PILLAR DEFORMATION

The capillary force and LaPlace force from the evaporating meniscus can be provided through the following equations, respectively.

$$F_c = \frac{-\pi\gamma R^2 \cos^2\theta}{\sqrt{(s/2)^2 - R^2}} \tag{C.1}$$

$$F_c = \frac{\gamma R H^2 \cos\theta}{(s/2) - R} \tag{C.2}$$

However, it can be determined that the LaPlace force is going to have a greater impact on the deformation of the pillar than the capillary force. This was reinforced by Chandra and Yang. Due to the cosine terms in the force, it can be said that the direction of the forced will be down parallel to the side of the pillar, creating a buckling force. Based on what is seen from the videos in the Supplemental File, this is consistent with what is observed. One can apply the critical force for buckling below

$$F_{crit} = \frac{n^2\pi^2 EI}{H^2} \tag{C.3}$$

where n is an effective length factor (0.5 for this case) and I is the moment of inertia for the structure. Relating the critical force for buckling to the LaPLace pressure yields the following equation.

$$E \sim \frac{16\gamma h^3 \cos^2\theta}{\pi r^3 (s/2 - R)} \tag{C.4}$$

The time scale has to be estimated based off of the evaporation rate of a fluid meniscus. First, a scale for the change in volume is developed with respect to the contact angle of the fluid from the pillar. This scale is expressed below

$$\Delta V = 2RH(s - 2R)(1 - \cos\theta) \tag{C.5}$$

Now the evaporating rate for an evaporating meniscus must be used to find the time scale of the change in volume. This evaporation rate can be scaled as

$$\dot{m} \sim \frac{k_f \Delta T}{\delta h_{fg}} \tag{C.6}$$

Combing the above two equations yields:

$$\dot{m} \sim \frac{\rho \Delta V}{\Delta t} \sim \frac{\rho 2RH(s-2R)(1-\cos\theta)}{\Delta t} \sim \frac{k_f \Delta T}{\delta h_{fg}} \tag{C.7}$$

Rearranging the above equations yields the following time scale for deformation:

$$t_{mod} \sim (1-\cos\theta)\frac{2\rho rh(s-2r)\delta h_{fg}}{k_f \Delta T} \tag{C.8}$$

APPENDIX D: METAMATERIALS ADDITIONAL INFORMATION

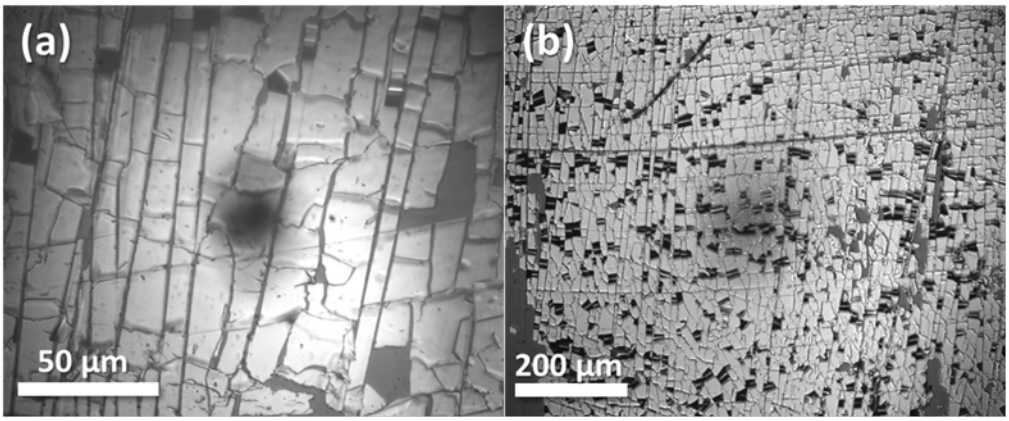

Figure D.1: A top view of the metamaterial Putty 44 using a (a) 5x infinity objective and a (b) 10 x infinity objective

APPENDIX E: SURFACE CHEMISTRY ADDITIONAL INFORMATION

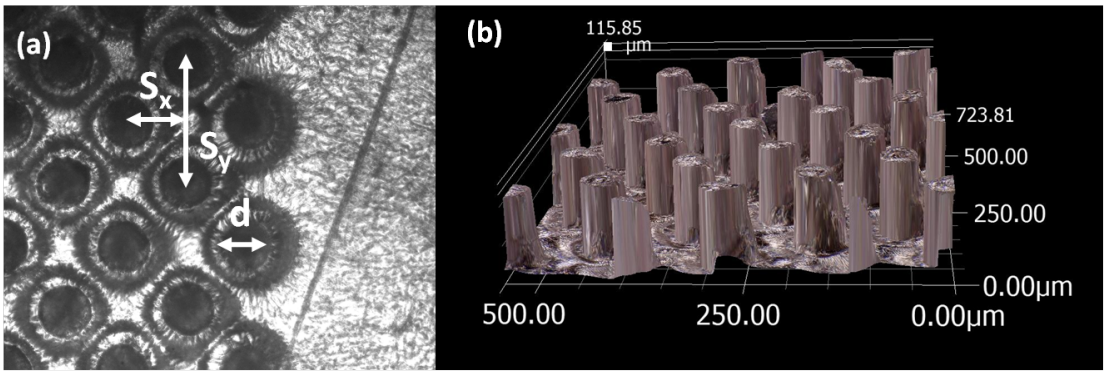

Figure E.1: (a) An overhead view of Sample A for the PVA experimentation along with the definitions of the wicking geometry (b) A 3D image of the microstructures of Sample D for the PVA experimentation

Table E.1: The Contact Angle Values (in Degrees) of Bare Gold Under 5 mM Concentration of Cystamine Dihydrochloride SAM

Condition	EDC	SPCOOH	EDC/SPCOOH
After SPCOOH Application	68.8 ± 1.52	74.3 ± 1.67	64.0 ± 1.88
1 min UV light	69.6 ± 1.86	76.2 ± 4.74	66.0 ± 2.20
10 min Vis light	71.4 ± 0.90	79.7 ± 5.24	68.8 ± 1.30

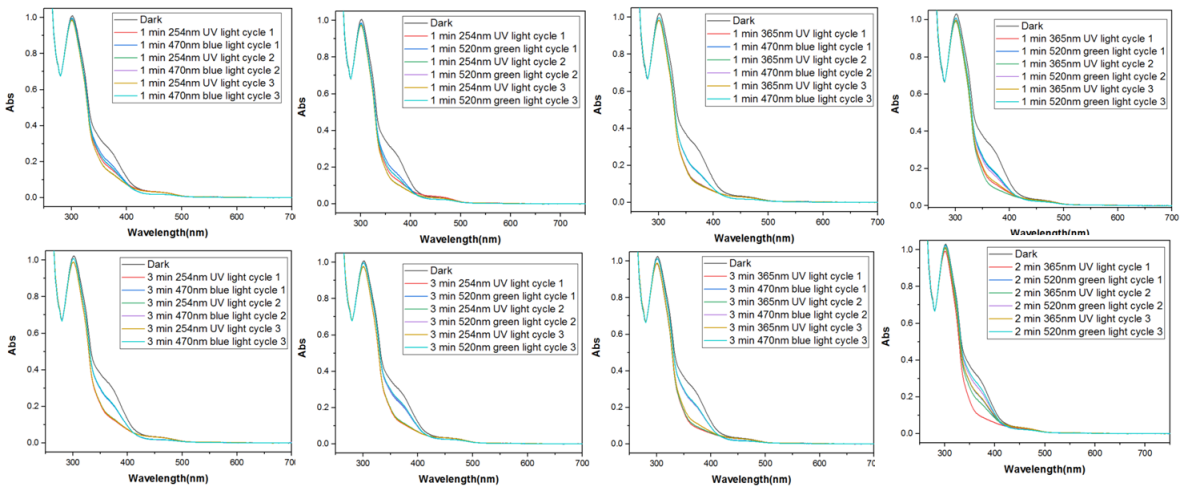

Figure E.2: The absorption of SPCOOH in ethanol under different light cycles. The four light cycles presented are 254 nm to 520 nm, 365 nm to 520 nm, 254 nm to 470 nm, and 365 nm to 470 nm. For each result, dark was used as a control to detect changes in the orientation of SPCOOH

Table E.2: The Contact Angle Values (in Degrees) of Bare Gold Under 50 mM Concentration of Cystamine Dihydrochloride SAM

Condition	EDC	SPCOOH	EDC/SPCOOH
After SPCOOH Application	72.8 ± 2.11	76.2 ± 4.74	73.7 ± 1.23
1 min UV light	69.5 ± 1.29	76.3 ± 1.21	73.8 ± 1.47
10 min Vis light	73.1 ± 1.86	76.9 ± 4.32	73.6 ± 1.13

APPENDIX F: COPYRIGHT PERMISSIONS

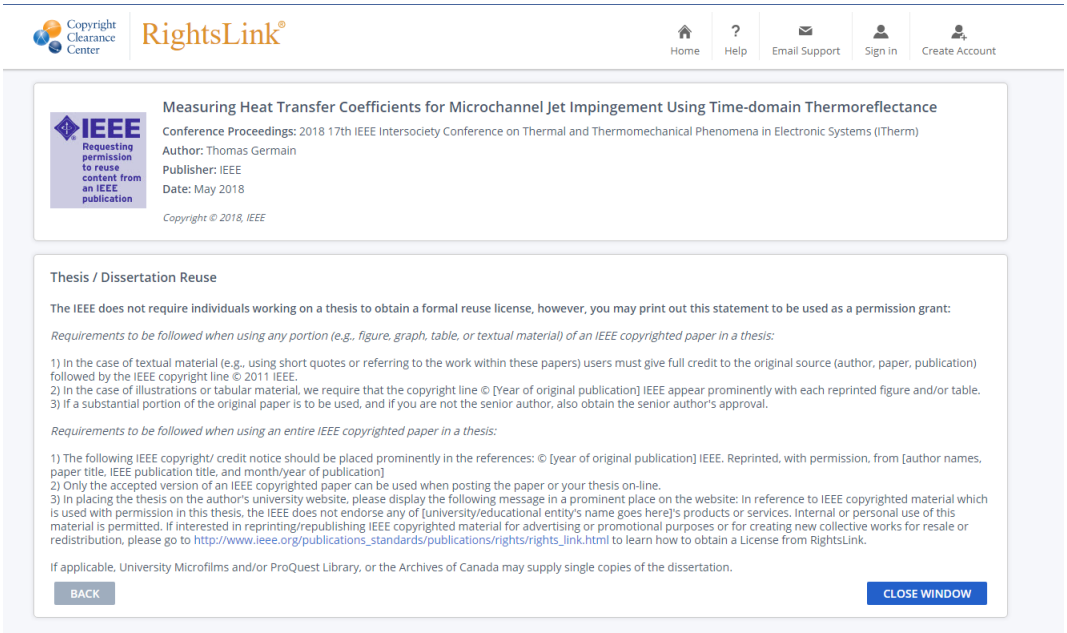

Figure F.1: The copyright permission from IEEE to use anything from my paper from the 2018 IEEE ITtherm Conference

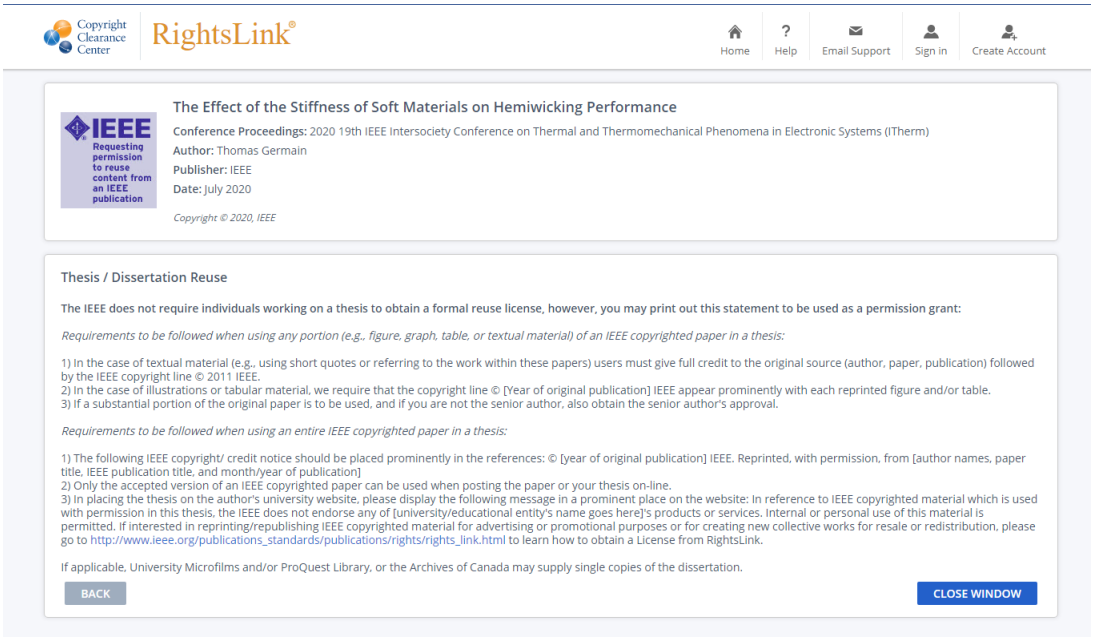

Figure F.2: The copyright permission from IEEE to use anything from my paper from the 2020 IEEE ITtherm Conference

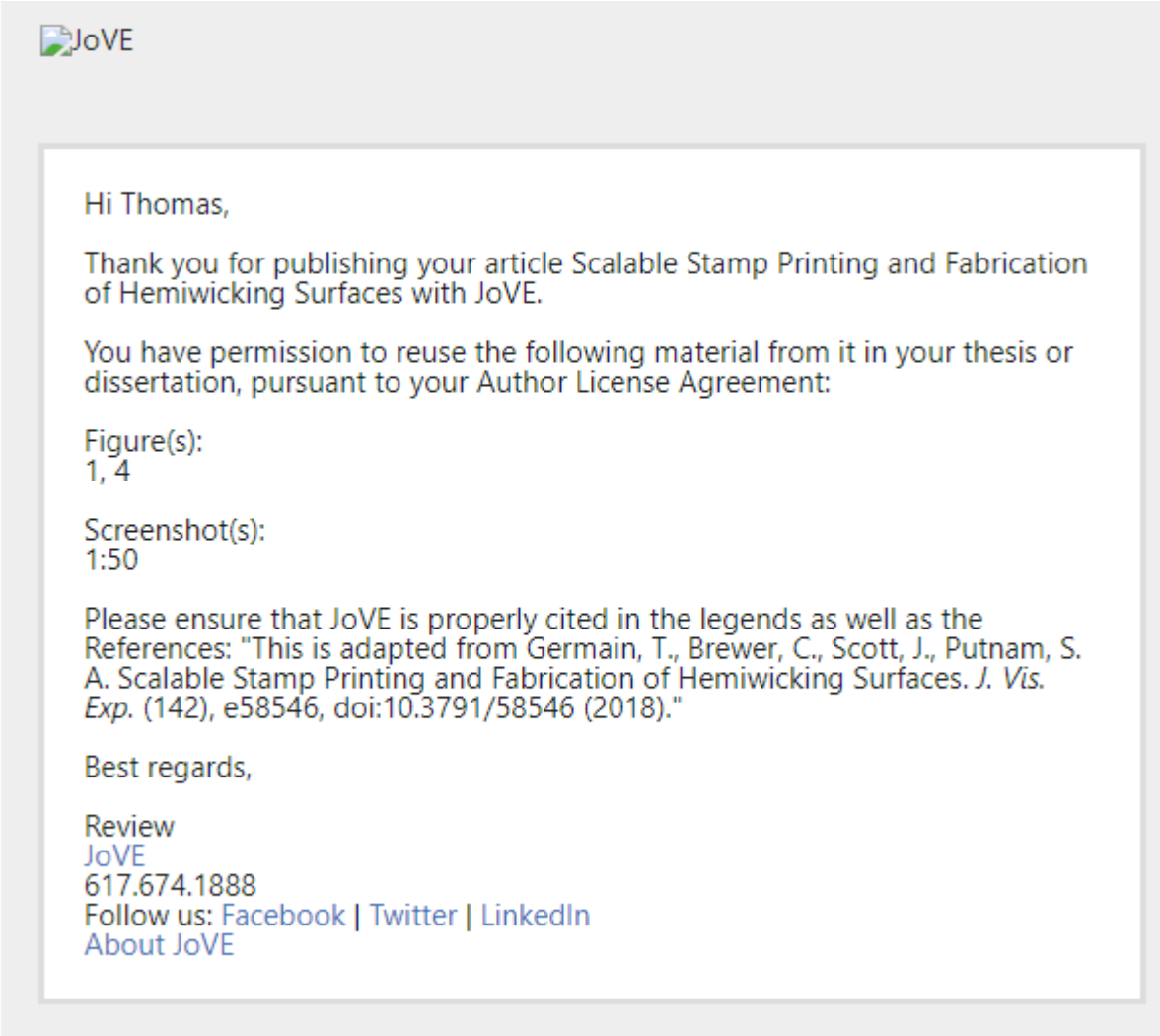

Figure F.3: The copyright permission from JoVE to use the following figures and videos from the submitted paper

LIST OF REFERENCES

[1] Tadhg S O'Donovan and Darina B Murray. Jet impingement heat transfer–part i: Mean and root-mean-square heat transfer and velocity distributions. *International journal of heat and mass transfer*, 50(17-18):3291–3301, 2007.

[2] Arash Azimi, Mehdi Ashjaee, and Pooyan Razi. Slot jet impingement cooling of a concave surface in an annulus. *Experimental Thermal and Fluid Science*, 68:300–309, 2015.

[3] Yuichi Mitsutake and Masanori Monde. Ultra high critical heat flux during forced flow boiling heat transfer with an impinging jet. *J. Heat Transfer*, 125(6):1038–1045, 2003.

[4] M Mitchell Waldrop. The chips are down for moore's law. *Nature News*, 530(7589):144, 2016.

[5] Chris A Mack. Fifty years of moore's law. *IEEE Transactions on semiconductor manufacturing*, 24(2):202–207, 2011.

[6] Mehrdad Mehrvand. Local transient characterization of thermofluid heat transfer coefficient at solid-liquid nano-interfaces. 2017.

[7] Tanvir Ahmed Chowdhury, Chance Brewer, and Shawn A Putnam. Hotspot cooling performance of a submerged water jet via infrared thermometry. In *2020 19th IEEE Intersociety Conference on Thermal and Thermomechanical Phenomena in Electronic Systems (ITherm)*, pages 166–172. IEEE, 2020.

[8] Matthew D Clark, Justin A Weibel, and Suresh V Garimella. Identification of the dominant heat transfer mechanisms during confined two-phase jet impingement. In *2018 17th IEEE Intersociety Conference on Thermal and Thermomechanical Phenomena in Electronic Systems (ITherm)*, pages 424–428. IEEE, 2018.

[9] Khan Md Rabbi, Christopher Borden, and Shawn A Putnam. A novel thermal mapping technique using nano-confinement assisted quantum dots for transient cooling applications. In *2020 19th IEEE Intersociety Conference on Thermal and Thermomechanical Phenomena in Electronic Systems (ITherm)*, pages 926–931. IEEE, 2020.

[10] Przemysław Smakulski and Sławomir Pietrowicz. A review of the capabilities of high heat flux removal by porous materials, microchannels and spray cooling techniques. *Applied Thermal Engineering*, 104:636–646, 2016.

[11] Ruey-Hung Chen, Louis C Chow, and Jose E Navedo. Effects of spray characteristics on critical heat flux in subcooled water spray cooling. *International Journal of Heat and Mass Transfer*, 45(19):4033–4043, 2002.

[12] Wen-Pin Hsieh, Bin Chen, Jie Li, Pawel Keblinski, and David G Cahill. Pressure tuning of the thermal conductivity of the layered muscovite crystal. *Physical Review B*, 80(18):180302, 2009.

[13] Gangtao Liang and Issam Mudawar. Review of spray cooling–part 1: Single-phase and nucleate boiling regimes, and critical heat flux. *International Journal of Heat and Mass Transfer*, 115:1174–1205, 2017.

[14] YB Tan, JL Xie, F Duan, TN Wong, KC Toh, KF Choo, PK Chan, and YS Chua. Multi-nozzle spray cooling for high heat flux applications in a closed loop system. *Applied thermal engineering*, 54(2):372–379, 2013.

[15] Yaqing Wang, Minghou Liu, Dong Liu, Kan Xu, and Yiliang Chen. Experimental study on the effects of spray inclination on water spray cooling performance in non-boiling regime. *Experimental Thermal and Fluid Science*, 34(7):933–942, 2010.

[16] MR Pais, LC Chow, and ET Mahefkey. Surface roughness and its effects on the heat transfer mechanism in spray cooling. 1992.

[17] Louis C Chow, Maninder S Sehmbey, and Martin R Pais. High heat flux spray cooling. *Annual Review of Heat Transfer*, 8, 1997.

[18] Gangtao Liang and Issam Mudawar. Review of spray cooling–part 2: High temperature boiling regimes and quenching applications. *International Journal of Heat and Mass Transfer*, 115:1206–1222, 2017.

[19] Will Libeer, Francisco Ramos, Chad Newton, Morteza Alipanahrostami, Chris Depcik, and Xianglin Li. Two-phase heat and mass transfer of phase change materials in thermal management systems. *International Journal of Heat and Mass Transfer*, 100:215–223, 2016.

[20] Chirag R Kharangate, Lucas E O'Neill, and Issam Mudawar. Effects of two-phase inlet quality, mass velocity, flow orientation, and heating perimeter on flow boiling in a rectangular channel: Part 1–two-phase flow and heat transfer results. *International journal of heat and mass transfer*, 103:1261–1279, 2016.

[21] Matthew D Clark, Justin A Weibel, and Suresh V Garimella. Identification of nucleate boiling as the dominant heat transfer mechanism during confined two-phase jet impingement. *International Journal of Heat and Mass Transfer*, 128:1095–1101, 2019.

[22] Hassam Nasarullah Chaudhry, Ben Richard Hughes, and Saud Abdul Ghani. A review of heat pipe systems for heat recovery and renewable energy applications. *Renewable and Sustainable Energy Reviews*, 16(4):2249–2259, 2012.

[23] Wasan Srimuang and Pipatana Amatachaya. A review of the applications of heat pipe heat exchangers for heat recovery. *Renewable and Sustainable Energy Reviews*, 16(6):4303–4315, 2012.

[24] Hussam Jouhara, Amisha Chauhan, Theodora Nannou, S Almahmoud, Bertrand Delpech, and Luiz C Wrobel. Heat pipe based systems-advances and applications. *Energy*, 128:729–754, 2017.

[25] Hamidreza Shabgard, Michael J Allen, Nourouddin Sharifi, Steven P Benn, Amir Faghri, and Theodore L Bergman. Heat pipe heat exchangers and heat sinks: Opportunities, challenges, applications, analysis, and state of the art. *International Journal of Heat and Mass Transfer*, 89:138–158, 2015.

[26] SB Riffat, X Zhao, and PS Doherty. Developing a theoretical model to investigate thermal performance of a thin membrane heat-pipe solar collector. *Applied Thermal Engineering*, 25(5-6):899–915, 2005.

[27] Mostafa A Abd El-Baky and Mousa M Mohamed. Heat pipe heat exchanger for heat recovery in air conditioning. *Applied thermal engineering*, 27(4):795–801, 2007.

[28] Jian Qu, Huiying Wu, Ping Cheng, Qian Wang, and Qin Sun. Recent advances in mems-based micro heat pipes. *International Journal of Heat and Mass Transfer*, 110:294–313, 2017.

[29] Chao Yang, Chengyi Song, Wen Shang, Peng Tao, and Tao Deng. Flexible heat pipes with integrated bioinspired design. *Progress in Natural Science: Materials International*, 25(1):51–57, 2015.

[30] Christopher Oshman, Qian Li, Li-Anne Liew, Ronggui Yang, Victor M Bright, and YC Lee. Flat flexible polymer heat pipes. *Journal of Micromechanics and Microengineering*, 23(1):015001, 2012.

[31] Chao Yang, Chao Chang, Chengyi Song, Wen Shang, Jianbo Wu, Peng Tao, and Tao Deng. Fabrication and performance evaluation of flexible heat pipes for potential thermal control of foldable electronics. *Applied Thermal Engineering*, 95:445–453, 2016.

[32] David E Glass, Jonathan C Stevens, and VV Raman. Flexible heat pipes for a lightweight spacecraft radiator. *Journal of Spacecraft and Rockets*, 36(5):711–718, 1999.

[33] Han Hu, Justin A Weibel, and Suresh V Garimella. Role of nanoscale roughness in the heat transfer characteristics of thin film evaporation. *International Journal of Heat and Mass Transfer*, 150:119306, 2020.

[34] Kyoungwoo Park and Kwan-Soo Lee. Flow and heat transfer characteristics of the evaporating extended meniscus in a micro-capillary channel. *International Journal of Heat and Mass Transfer*, 46(24):4587–4594, 2003.

[35] Sashidhar S Panchamgam, Arya Chatterjee, Joel L Plawsky, and Peter C Wayner Jr. Comprehensive experimental and theoretical study of fluid flow and heat transfer in a microscopic evaporating meniscus in a miniature heat exchanger. *International Journal of Heat and Mass Transfer*, 51(21-22):5368–5379, 2008.

[36] Cheng-Kang Guan, Bradley Bon, James Klausner, and Renwei Mei. Comparison of chf enhancement on microstructured surfaces with a predictive model. *Heat transfer engineering*, 35(5):452–460, 2014.

[37] Q Li, Y Yu, P Zhou, and HJ Yan. Enhancement of boiling heat transfer using hydrophilic-hydrophobic mixed surfaces: A lattice boltzmann study. *Applied Thermal Engineering*, 132:490–499, 2018.

[38] Zhenbin Ge, David G Cahill, and Paul V Braun. Thermal conductance of hydrophilic and hydrophobic interfaces. *Physical review letters*, 96(18):186101, 2006.

[39] C Ding, G Soni, P Bozorgi, CD Meinhart, and NC MacDonald. Wicking study of nanostructured titania surfaces for flat heat pipes. In *Nanotech Conference & Expo, Houston, TX*, 2009.

[40] Misheck G Mwaba, Xiao Huang, and Junjie Gu. Influence of wick characteristics on heat pipe performance. *International journal of energy research*, 30(7):489–499, 2006.

[41] Glen McHale, Michael I Newton, and Neil J Shirtcliffe. Dynamic wetting and spreading and the role of topography. *Journal of Physics: Condensed Matter*, 21(46):464122, 2009.

[42] Yangying Zhu, Dion S Antao, Zhengmao Lu, Sivanand Somasundaram, Tiejun Zhang, and Evelyn N Wang. Prediction and characterization of dry-out heat flux in micropillar wick structures. *Langmuir*, 32(7):1920–1927, 2016.

[43] Beom Seok Kim, Geehong Choi, Dong Il Shim, Kyung Min Kim, and Hyung Hee Cho. Surface roughening for hemi-wicking and its impact on convective boiling heat transfer. *International Journal of Heat and Mass Transfer*, 102:1100–1107, 2016.

[44] Mehrdad Mehrvand and Shawn A Putnam. Probing the local heat transfer coefficient of water-cooled microchannels using time-domain thermoreflectance. *Journal of Heat Transfer*, 139(11), 2017.

[45] N Zuckerman and N Lior. Jet impingement heat transfer: physics, correlations, and numerical modeling. *Advances in heat transfer*, 39:565–631, 2006.

[46] AJ Robinson and E Schnitzler. An experimental investigation of free and submerged miniature liquid jet array impingement heat transfer. *Experimental Thermal and Fluid Science*, 32(1):1–13, 2007.

[47] V Narayanan, J Seyed-Yagoobi, and RH Page. An experimental study of fluid mechanics and heat transfer in an impinging slot jet flow. *International Journal of Heat and Mass Transfer*, 47(8-9):1827–1845, 2004.

[48] Colin Glynn, Tadhg O'Donovan, Darina B Murray, and M Feidt. Jet impingement cooling. In *Proceedings of the 9th UK National Heat Transfer Conference*, pages 5–6, 2005.

[49] Nitin Karwa, Tatiana Gambaryan-Roisman, Peter Stephan, and Cameron Tropea. Experimental investigation of circular free-surface jet impingement quenching: transient hydrodynamics and heat transfer. *Experimental thermal and fluid science*, 35(7):1435–1443, 2011.

[50] W Timm, K Weinzierl, and A Leipertz. Heat transfer in subcooled jet impingement boiling at high wall temperatures. *International journal of heat and mass transfer*, 46(8):1385–1393, 2003.

[51] CF Ma, YP Gan, YC Tian, DH Lei, and T Gomi. Liquid jet impingement heat transfer with or without boiling. *Journal of Thermal Science*, 2(1):32, 1993.

[52] Suresh V Garimella and Boris Nenaydykh. Nozzle-geometry effects in liquid jet impingement heat transfer. *International Journal of Heat and Mass Transfer*, 39(14):2915–2923, 1996.

[53] Puneet Gulati, Vadiraj Katti, and SV Prabhu. Influence of the shape of the nozzle on local heat transfer distribution between smooth flat surface and impinging air jet. *International Journal of Thermal Sciences*, 48(3):602–617, 2009.

[54] Yue-Tzu Yang, Yi-Hsien Wang, and Jen-Chi Hsu. Numerical thermal analysis and optimization of a water jet impingement cooling with vof two-phase approach. *International Communications in Heat and Mass Transfer*, 68:162–171, 2015.

[55] Tae Seon Park and Hyung Jin Sung. Development of a near-wall turbulence model and application to jet impingement heat transfer. *International journal of heat and fluid flow*, 22(1):10–18, 2001.

[56] M Behnia, S Parneix, Y Shabany, and PA Durbin. Numerical study of turbulent heat transfer in confined and unconfined impinging jets. *International Journal of Heat and Fluid Flow*, 20(1):1–9, 1999.

[57] JW Baughn and S Shimizu. Heat transfer measurements from a surface with uniform heat flux and an impinging jet. *Journal of Heat Transfer (Transactions of the ASME (American Society of Mechanical Engineers), Series C);(United States)*, 111(4), 1989.

[58] James W Baughn, Anthony E Hechanova, and Xiaojun Yan. An experimental study of entrainment effects on the heat transfer from a flat surface to a heated circular impinging jet. *Journal of Heat Transfer (Transactions of the ASME (American Society of Mechanical Engineers), Series C);(United States)*, 113(4), 1991.

[59] Yan Xiaojun. A preheated-wall transient method using liquid crystals for the measurement of heat transfer on external surfaces and in ducts. *Previews of Heat and Mass Transfer*, 5(21):459–460, 1995.

[60] David G Cahill. Analysis of heat flow in layered structures for time-domain thermoreflectance. *Review of scientific instruments*, 75(12):5119–5122, 2004.

[61] Kwangu Kang, Yee Kan Koh, Catalin Chiritescu, Xuan Zheng, and David G Cahill. Two-tint pump-probe measurements using a femtosecond laser oscillator and sharp-edged optical filters. *Review of Scientific Instruments*, 79(11):114901, 2008.

[62] Aaron Schmidt, Matteo Chiesa, Xiaoyuan Chen, and Gang Chen. An optical pump-probe technique for measuring the thermal conductivity of liquids. *Review of Scientific Instruments*, 79(6):064902, 2008.

[63] Yee Kan Koh and David G Cahill. Frequency dependence of the thermal conductivity of semiconductor alloys. *Physical Review B*, 76(7):075207, 2007.

[64] Thomas Germain, Tanvir A Chowdhury, Jake Carter, and Shawn A Putnam. Measuring heat transfer coefficients for microchannel jet impingement using time-domain thermoreflectance. In *2018 17th IEEE Intersociety Conference on Thermal and Thermomechanical Phenomena in Electronic Systems (ITherm)*, pages 449–454. IEEE, 2018.

[65] YC Chen, CF Ma, M Qin, and YX Li. Theoretical study on impingement heat transfer with single-phase free-surface slot jets. *International journal of heat and mass transfer*, 48(16):3381–3386, 2005.

[66] John H Lienhard. Heat transfer by impingement of circular free-surface liquid jets. In *18th National and 7th ISHMT-ASME, Heat and Mass Transfer Conference, Guwahati, India*, 2006.

[67] TA Otitoju, AL Ahmad, and BS Ooi. Superhydrophilic (superwetting) surfaces: A review on fabrication and application. *Journal of industrial and engineering chemistry*, 47:19–40, 2017.

[68] HangJin Jo, Ho Seon Ahn, SoonHo Kang, and Moo Hwan Kim. A study of nucleate boiling heat transfer on hydrophilic, hydrophobic and heterogeneous wetting surfaces. *International Journal of Heat and Mass Transfer*, 54(25-26):5643–5652, 2011.

[69] Yuehua Yuan and T Randall Lee. Contact angle and wetting properties. In *Surface science techniques*, pages 3–34. Springer, 2013.

[70] José Bico, Uwe Thiele, and David Quéré. Wetting of textured surfaces. *Colloids and Surfaces A: Physicochemical and Engineering Aspects*, 206(1-3):41–46, 2002.

[71] Dimitri Janssen, Randy De Palma, Stijn Verlaak, Paul Heremans, and Wim Dehaen. Static solvent contact angle measurements, surface free energy and wettability determination of various self-assembled monolayers on silicon dioxide. *Thin Solid Films*, 515(4):1433–1438, 2006.

[72] Hai Trieu Phan, Nadia Caney, Philippe Marty, Stéphane Colasson, and Jérôme Gavillet. Surface wettability control by nanocoating: the effects on pool boiling heat transfer and nucleation mechanism. *International Journal of Heat and Mass Transfer*, 52(23-24):5459–5471, 2009.

[73] Hans-Jürgen Butt, Dmytro S Golovko, and Elmar Bonaccurso. On the derivation of young's equation for sessile drops: nonequilibrium effects due to evaporation. *The Journal of Physical Chemistry B*, 111(19):5277–5283, 2007.

[74] Johnathan S Coursey and Jungho Kim. Nanofluid boiling: The effect of surface wettability. *International Journal of Heat and Fluid Flow*, 29(6):1577–1585, 2008.

[75] Takanori Shimizu, Tatsuro Goda, Norihiko Minoura, Madoka Takai, and Kazuhiko Ishihara. Super-hydrophilic silicone hydrogels with interpenetrating poly (2-methacryloyloxyethyl phosphorylcholine) networks. *Biomaterials*, 31(12):3274–3280, 2010.

[76] KJ Kubiak, MCT Wilson, TG Mathia, and Ph Carval. Wettability versus roughness of engineering surfaces. *Wear*, 271(3-4):523–528, 2011.

[77] AM Cazabat and MA Cohen Stuart. Dynamics of wetting: effects of surface roughness. *The Journal of Physical Chemistry*, 90(22):5845–5849, 1986.

[78] Junaid Ali Syed, Shaochun Tang, and Xiangkang Meng. Super-hydrophobic multilayer coatings with layer number tuned swapping in surface wettability and redox catalytic anti-corrosion application. *Scientific reports*, 7(1):1–17, 2017.

[79] Wonjae Choi, Anish Tuteja, Joseph M Mabry, Robert E Cohen, and Gareth H McKinley. A modified cassie–baxter relationship to explain contact angle hysteresis and anisotropy on non-wetting textured surfaces. *Journal of colloid and interface science*, 339(1):208–216, 2009.

[80] Daiki Murakami, Hiroshi Jinnai, and Atsushi Takahara. Wetting transition from the cassie–baxter state to the wenzel state on textured polymer surfaces. *Langmuir*, 30(8):2061–2067, 2014.

[81] Edward Bormashenko, Roman Pogreb, Gene Whyman, and Mordehai Erlich. Cassie- wenzel wetting transition in vibrating drops deposited on rough surfaces: Is the dynamic cassie-wenzel wetting transition a 2d or 1d affair? *Langmuir*, 23(12):6501–6503, 2007.

[82] Edward Bormashenko, Roman Pogreb, Gene Whyman, Yelena Bormashenko, and Mordechai Erlich. Vibration-induced cassie-wenzel wetting transition on rough surfaces. *Applied physics letters*, 90(20):201917, 2007.

[83] Anne-Marie Kietzig, Mehr Negar Mirvakili, Saeid Kamal, Peter Englezos, and Savvas G Hatzikiriakos. Laser-patterned super-hydrophobic pure metallic substrates: Cassie to wenzel wetting transitions. *Journal of Adhesion Science and Technology*, 25(20):2789–2809, 2011.

[84] Beom Seok Kim, Hwanseong Lee, Sangwoo Shin, Geehong Choi, and Hyung Hee Cho. Interfacial wicking dynamics and its impact on critical heat flux of boiling heat transfer. *Applied Physics Letters*, 105(19):191601, 2014.

[85] Ran Li and Zhongwei Huang. A new chf model for enhanced pool boiling heat transfer on surfaces with micro-scale roughness. *International Journal of Heat and Mass Transfer*, 109:1084–1093, 2017.

[86] Jungchul Kim, Myoung-Woon Moon, and Ho-Young Kim. Dynamics of hemiwicking. *Journal of Fluid Mechanics*, 800:57–71, 2016.

[87] Siva Rama Krishnan, John Bal, and Shawn A Putnam. A simple analytic model for predicting the wicking velocity in micropillar arrays. *Scientific Reports*, 9(1):1–9, 2019.

[88] Ilya Levental, Penelope C Georges, and Paul A Janmey. Soft biological materials and their impact on cell function. *Soft Matter*, 3(3):299–306, 2007.

[89] Mark Geoghegan and Georg Krausch. Wetting at polymer surfaces and interfaces. *Progress in Polymer Science*, 28(2):261–302, 2003.

[90] Berend-Jan de Gans and Ulrich S Schubert. Inkjet printing of well-defined polymer dots and arrays. *Langmuir*, 20(18):7789–7793, 2004.

[91] Zhen Cao, Mark J Stevens, and Andrey V Dobrynin. Adhesion and wetting of nanoparticles on soft surfaces. *Macromolecules*, 47(9):3203–3209, 2014.

[92] Longquan Chen, Günter K Auernhammer, and Elmar Bonaccurso. Short time wetting dynamics on soft surfaces. *Soft Matter*, 7(19):9084–9089, 2011.

[93] Julia Gerber, Tobias Lendenmann, Hadi Eghlidi, Thomas M Schutzius, and Dimos Poulikakos. Wetting transitions in droplet drying on soft materials. *Nature communications*, 10(1):1–10, 2019.

[94] MER Shanahan and A Carre. Viscoelastic dissipation in wetting and adhesion phenomena. *Langmuir*, 11(4):1396–1402, 1995.

[95] Marcus C Lopes and Elmar Bonaccurso. Evaporation control of sessile water drops by soft viscoelastic surfaces. *Soft Matter*, 8(30):7875–7881, 2012.

[96] Gang Pu and Steven J Severtson. Water evaporation on highly viscoelastic polymer surfaces. *Langmuir*, 28(26):10007–10014, 2012.

[97] Su Ji Park, Byung Mook Weon, Ji San Lee, Junho Lee, Jinkyung Kim, and Jung Ho Je. Visualization of asymmetric wetting ridges on soft solids with x-ray microscopy. *Nature communications*, 5(1):1–7, 2014.

[98] Robert W Style, Rostislav Boltyanskiy, Yonglu Che, JS Wettlaufer, Larry A Wilen, and Eric R Dufresne. Universal deformation of soft substrates near a contact line and the direct measurement of solid surface stresses. *Physical review letters*, 110(6):066103, 2013.

[99] Longquan Chen, Elmar Bonaccurso, Tatiana Gambaryan-Roisman, Victor Starov, Nektaria Koursari, and Yapu Zhao. Static and dynamic wetting of soft substrates. *Current opinion in colloid & interface science*, 36:46–57, 2018.

[100] Joshua B Bostwick, Michael Shearer, and Karen E Daniels. Elastocapillary deformations on partially-wetting substrates: rival contact-line models. *Soft Matter*, 10(37):7361–7369, 2014.

[101] Robert W Style and Eric R Dufresne. Static wetting on deformable substrates, from liquids to soft solids. *Soft Matter*, 8(27):7177–7184, 2012.

[102] SJ Park, JB Bostwick, V De Andrade, and JH Je. Self-spreading of the wetting ridge during stick-slip on a viscoelastic surface. *Soft Matter*, 13(44):8331–8336, 2017.

[103] Robert W Style, Anand Jagota, Chung-Yuen Hui, and Eric R Dufresne. Elastocapillarity: Surface tension and the mechanics of soft solids. *Annual Review of Condensed Matter Physics*, 8:99–118, 2017.

[104] Ying-song Yu. Substrate elastic deformation due to vertical component of liquid-vapor interfacial tension. *Applied Mathematics and Mechanics*, 33(9):1095–1114, 2012.

[105] Alexandru Mihai Grumezescu. *Lipid Nanocarriers for Drug Targeting*. William Andrew, 2018.

[106] JA Diez, R Gratton, LP Thomas, and B Marino. Laplace pressure driven drop spreading. *Physics of Fluids*, 6(1):24–33, 1994.

[107] Siyan Deng, Weifeng Shang, Shile Feng, Shiping Zhu, Yan Xing, Dan Li, Yongping Hou, and Yongmei Zheng. Controlled droplet transport to target on a high adhesion surface with multi-gradients. *Scientific reports*, 7:45687, 2017.

[108] Tian-Le Cheng and Yu U Wang. Shape-anisotropic particles at curved fluid interfaces and role of laplace pressure: A computational study. *Journal of colloid and interface science*, 402:267–278, 2013.

[109] Rafael D Schulman and Kari Dalnoki-Veress. Liquid droplets on a highly deformable membrane. *Physical review letters*, 115(20):206101, 2015.

[110] Benoit Roman and José Bico. Elasto-capillarity: deforming an elastic structure with a liquid droplet. *Journal of Physics: Condensed Matter*, 22(49):493101, 2010.

[111] Dinesh Chandra and Shu Yang. Capillary-force-induced clustering of micropillar arrays: is it caused by isolated capillary bridges or by the lateral capillary meniscus interaction force? *Langmuir*, 25(18):10430–10434, 2009.

[112] Pierre-Gilles De Gennes. Wetting: statics and dynamics. *Reviews of modern physics*, 57(3):827, 1985.

[113] Anne-Laure Biance, Christophe Clanet, and David Quéré. First steps in the spreading of a liquid droplet. *Physical Review E*, 69(1):016301, 2004.

[114] Antonin Eddi, Koen G Winkels, and Jacco H Snoeijer. Short time dynamics of viscous drop spreading. *Physics of fluids*, 25(1):013102, 2013.

[115] Koen G Winkels, Joost H Weijs, Antonin Eddi, and Jacco H Snoeijer. Initial spreading of low-viscosity drops on partially wetting surfaces. *Physical Review E*, 85(5):055301, 2012.

[116] Bruno Andreotti and Jacco H Snoeijer. Statics and dynamics of soft wetting. *Annual Review of Fluid Mechanics*, 52, 2020.

[117] Gang Pu and Steven J Severtson. Characterization of dynamic stick-and-break wetting behavior for various liquids on the surface of a highly viscoelastic polymer. *Langmuir*, 24(9):4685–4692, 2008.

[118] Mathijs van Gorcum, Bruno Andreotti, Jacco H Snoeijer, and Stefan Karpitschka. Dynamic solid surface tension causes droplet pinning and depinning. *Physical review letters*, 121(20):208003, 2018.

[119] Stefan Karpitschka, Anupam Pandey, Luuk A Lubbers, Joost H Weijs, Lorenzo Botto, Siddhartha Das, Bruno Andreotti, and Jacco H Snoeijer. Liquid drops attract or repel by the inverted cheerios effect. *Proceedings of the National Academy of Sciences*, 113(27):7403–7407, 2016.

[120] Menghua Zhao, Julien Dervaux, Tetsuharu Narita, François Lequeux, Laurent Limat, and Matthieu Roché. Geometrical control of dissipation during the spreading of liquids on soft solids. *Proceedings of the National Academy of Sciences*, 115(8):1748–1753, 2018.

[121] Thomas Germain, Chance Brewer, James Scott, and Shawn A Putnam. Scalable stamp printing and fabrication of hemiwicking surfaces. *JoVE (Journal of Visualized Experiments)*, (142):e58546, 2018.

[122] Morten Bo Mikkelsen, Rodolphe Marie, Jan H Hansen, Dorota Wencel, Colette McDonagh, Hans Ole Nielsen, and Anders Kristensen. Controlled deposition of sol–gel sensor material using hemiwicking. *Journal of Micromechanics and Microengineering*, 21(11):115008, 2011.

[123] Tomi Haatainen and Jouni Ahopelto. Pattern transfer using step&stamp imprint lithography. *Physica Scripta*, 67(4):357, 2003.

[124] Stephen Y Chou, Peter R Krauss, and Preston J Renstrom. Nanoimprint lithography. *Journal of Vacuum Science & Technology B: Microelectronics and Nanometer Structures Processing, Measurement, and Phenomena*, 14(6):4129–4133, 1996.

[125] Alessandro Pozzato, Simone Dal Zilio, Giovanni Fois, Diego Vendramin, Giampaolo Mistura, Michele Belotti, Yong Chen, and Marco Natali. Superhydrophobic surfaces fabricated by nanoimprint lithography. *Microelectronic Engineering*, 83(4-9):884–888, 2006.

[126] Rahul Premachandran Nair and Min Zou. Surface-nano-texturing by aluminum-induced crystallization of amorphous silicon. *Surface and Coatings Technology*, 203(5-7):675–679, 2008.

[127] Jungchul Kim and Ho-Young Kim. On the dynamics of capillary imbibition. *Journal of mechanical science and technology*, 26(12):3795–3801, 2012.

[128] AA Arends, TM Germain, JF Owens, and SA Putnam. Simultaneous reflectometry and interferometry for measuring thin-film thickness and curvature. *Review of Scientific Instruments*, 89(5):055117, 2018.

[129] Lorenzo Ferrari, Chihhui Wu, Dominic Lepage, Xiang Zhang, and Zhaowei Liu. Hyperbolic metamaterials and their applications. *Progress in Quantum Electronics*, 40:1–40, 2015.

[130] Prashant Shekhar, Jonathan Atkinson, and Zubin Jacob. Hyperbolic metamaterials: fundamentals and applications. *Nano convergence*, 1(1):14, 2014.

[131] Ruben Maas, James Parsons, Nader Engheta, and Albert Polman. Experimental realization of an epsilon-near-zero metamaterial at visible wavelengths. *Nature Photonics*, 7(11):907–912, 2013.

[132] David R Smith, John B Pendry, and Mike CK Wiltshire. Metamaterials and negative refractive index. *Science*, 305(5685):788–792, 2004.

[133] Constantin Simovski, Stanislav Maslovski, Igor Nefedov, and Sergei Tretyakov. Optimization of radiative heat transfer in hyperbolic metamaterials for thermophotovoltaic applications. *Optics express*, 21(12):14988–15013, 2013.

[134] Fei Chen and Dang Yuan Lei. Experimental realization of extreme heat flux concentration with easy-to-make thermal metamaterials. *Scientific reports*, 5:11552, 2015.

[135] Hans-Jürgen Butt, Brunero Cappella, and Michael Kappl. Force measurements with the atomic force microscope: Technique, interpretation and applications. *Surface science reports*, 59(1-6):1–152, 2005.

[136] JN Israelachvili. Intermolecular and surface forces. academic press, london. *Intermolecular and surface forces. 2nd ed. Academic Press, London.*, 1992.

[137] Fritz London. The general theory of molecular forces. *Transactions of the Faraday Society*, 33:8b–26, 1937.

[138] Sean Eichenlaub, Carly Chan, and Stephen P Beaudoin. Hamaker constants in integrated circuit metalization. *Journal of Colloid and Interface Science*, 248(2):389–397, 2002.

[139] Hugo C Hamaker. The london—van der waals attraction between spherical particles. *physica*, 4(10):1058–1072, 1937.

[140] MA Noginov, Yuri A Barnakov, Vladimir Liberman, Srujana Prayakarao, Carl E Bonner, and Evgenii E Narimanov. Long-range wetting transparency on top of layered metal-dielectric substrates. *Scientific reports*, 6:27834, 2016.

[141] Vanessa N Peters, Srujana Prayakarao, Samantha R Koutsares, Carl E Bonner, and Mikhail A Noginov. Control of physical and chemical processes with nonlocal metal–dielectric environments. *ACS Photonics*, 2019.

[142] Parth K Patel, Juan E Arias, Renan S Gongora, Florencio E Hernandez, Aurélien Moncomble, Stéphane Aloïse, and Karin Y Chumbimuni-Torres. Visible light-triggered fluorescence and ph modulation using metastable-state photoacids and bodipy. *Physical Chemistry Chemical Physics*, 20(42):26804–26808, 2018.

[143] Garry Sinawang, Bing Wu, Jilei Wang, Shang Li, and Yaning He. Polystyrene based visible light responsive polymer with donor–acceptor stenhouse adduct pendants. *Macromolecular Chemistry and Physics*, 217(21):2409–2414, 2016.

[144] Rohit Rosario, Devens Gust, Antonio A Garcia, Mark Hayes, JL Taraci, T Clement, JW Dailey, and ST Picraux. Lotus effect amplifies light-induced contact angle switching. *The Journal of Physical Chemistry B*, 108(34):12640–12642, 2004.

[145] Shoichi Hayashida, Hirotsugu Sato, and Shungo Sugawara. Photo-induced wettability change in films containing spiropyran microcrystals. *Polymer journal*, 18(3):227–235, 1986.

[146] Eleonora Russo-Averchi, Jelena Vukajlovic Plestina, Gozde Tutuncuoglu, Federico Matteini, Anna Dalmau-Mallorquí, Maria De La Mata, Daniel Ruffer, Heidi A Potts, Jordi Arbiol, Sonia Conesa-Boj, et al. High yield of gaas nanowire arrays on si mediated by the pinning and contact angle of ga. *Nano letters*, 15(5):2869–2874, 2015.

[147] Rohit Rosario, Devens Gust, Mark Hayes, Frank Jahnke, Joseph Springer, and Antonio A Garcia. Photon-modulated wettability changes on spiropyran-coated surfaces. *Langmuir*, 18(21):8062–8069, 2002.

[148] Shiyang Jia, Angel Tan, Adrian Hawley, Bim Graham, and Ben J Boyd. Visible light-triggered cargo release from donor acceptor stenhouse adduct (dasa)-doped lyotropic liquid crystalline nanoparticles. *Journal of colloid and interface science*, 548:151–159, 2019.

[149] Robert J Byrne, Shannon E Stitzel, and Dermot Diamond. Photo-regenerable surface with potential for optical sensing. *Journal of Materials Chemistry*, 16(14):1332–1337, 2006.

[150] Bo Liao, Peng Long, Benqiao He, Shoujun Yi, Baoli Ou, Shaohua Shen, and Jian Chen. Reversible fluorescence modulation of spiropyran-functionalized carbon nanoparticles. *Journal of Materials Chemistry C*, 1(23):3716–3721, 2013.

[151] Antonio Garcia, Manuel Marquez, Tong Cai, Rohit Rosario, Zhibing Hu, Devens Gust, Mark Hayes, Sean A Vail, and Choong-Do Park. Photo-, thermally, and ph-responsive microgels. *Langmuir*, 23(1):224–229, 2007.

[152] Sergey Gorelik, Song Hongyan, Martin J Lear, and Jonathan Hobley. Transient brewster angle reflectometry of spiropyran monolayers. *Photochemical & Photobiological Sciences*, 9(2):141–151, 2010.

[153] Haiquan Zhao, Dongsheng Wang, Yue Fan, Mingrui Ren, Shumin Dong, and Yonghao Zheng. Surface with reversible green-light-switched wettability by donor–acceptor stenhouse adducts. *Langmuir*, 34(50):15537–15543, 2018.

[154] Lili Wang, Qi Wen, Pan Jia, Meijuan Jia, Diannan Lu, Xiaoming Sun, Lei Jiang, and Wei Guo. Light-driven active proton transport through photoacid-and photobase-doped janus graphene oxide membranes. *Advanced Materials*, 31(36):1903029, 2019.

[155] James Owens. Characteristics of hydrogel-wetted thin films. 2017.

[156] Armando Arends-Rodriguez. Implementation of optical interferometry and spectral reflectometry for high fidelity thin film measurements. 2017.